AGU100 ADVANCING EARTH AND SPACE SCIENCE

JGR Oceans

RESEARCH ARTICLE

10.1029/2019JC015101

Arctic Ocean Response to Greenland Sea Wind Anomalies in a Suite of Model Simulations

Morven Muilwijk[1,2], Mehmet Ilicak[3], Sam B. Cornish[4], Sergey Danilov[5], Renske Gelderloos[6], Rüdiger Gerdes[5], Verena Haid[7], Thomas W. N. Haine[6], Helen L. Johnson[4], Yavor Kostov[8], Tamás Kovács[5], Camille Lique[7], Juliana M. Marson[9], Paul G. Myers[9], Jeffery Scott[1,10], Lars H. Smedsrud[1,2,11], Claude Talandier[7], and Qiang Wang[5]

[1]Geophysical Institute, University of Bergen, Bergen, Norway, [2]Bjerknes Centre for Climate Research, Bergen, Norway, [3]Eurasia Institute of Earth Sciences, Istanbul Technical University, Istanbul, Turkey, [4]Department of Earth Sciences, University of Oxford, Oxford, UK , [5]Alfred-Wegener-Institut Helmholtz-Zentrum für Polar- und Meeresforschung, Bremerhaven, Germany, [6]Department of Earth and Planetary Sciences, The Johns Hopkins University, Baltimore, USA, [7]Laboratoire d'Océanographie Physique et Spatiale, Univ. Brest, CNRS, IRD, Ifremer, IUEM, Brest, France, [8]Department of Physics, University of Oxford, Oxford, UK, [9]Department of Earth and Atmospheric Sciences, University of Alberta, Edmonton, Alberta, Canada, [10]Department of Earth, Atmospheric and Planetary Sciences, Massachusetts Institute of Technology, Cambridge, MA, USA, [11]University Centre in Svalbard, Longyearbyen, Svalbard, Norway

Abstract Multimodel Arctic Ocean "climate response function" experiments are analyzed in order to explore the effects of anomalous wind forcing over the Greenland Sea (GS) on poleward ocean heat transport, Atlantic Water (AW) pathways, and the extent of Arctic sea ice. Particular emphasis is placed on the sensitivity of the AW circulation to anomalously strong or weak GS winds in relation to natural variability, the latter manifested as part of the North Atlantic Oscillation. We find that anomalously strong (weak) GS wind forcing, comparable in strength to a strong positive (negative) North Atlantic Oscillation index, results in an intensification (weakening) of the poleward AW flow, extending from south of the North Atlantic Subpolar Gyre, through the Nordic Seas, and all the way into the Canadian Basin. Reconstructions made utilizing the calculated climate response functions explain ~50% of the simulated AW flow variance; this is the proportion of variability that can be explained by GS wind forcing. In the Barents and Kara Seas, there is a clear relationship between the wind-driven anomalous AW inflow and the sea ice extent. Most of the anomalous AW heat is lost to the atmosphere, and loss of sea ice in the Barents Sea results in even more heat loss to the atmosphere, and thus effective ocean cooling. Release of passive tracers in a subset of the suite of models reveals differences in circulation patterns and shows that the flow of AW in the Arctic Ocean is highly dependent on the wind stress in the Nordic Seas.

Plain Language Summary The North Atlantic Current is an extension of the Gulf Stream, which brings warm Atlantic Water northward as the current flows through the Nordic Seas. Eventually, it enters the cold deep Arctic Ocean basins through the Barents Sea and Fram Strait. Nine different numerical ocean ice models have been analyzed and compared in order to investigate (1) their ability to simulate this northward flow of Atlantic Water, (2) its dependence on wind forcing, and (3) its impact on Arctic sea ice. Consistently, in all models, stronger winds in the Greenland Sea result in a stronger northward flow of warm Atlantic Water. The response on ocean circulation occurs from the North Atlantic, through the Nordic Seas and the Barents Sea, to the deep Canadian Basin. The flow of warm Atlantic Water within the Arctic Ocean is thus highly dependent on the wind stress in the Nordic Seas. There is particularly clear response in the Barents and Kara Seas where a wind-driven anomalous warm inflow drives a smaller sea ice extent and thickness, and an increased heat transfer from the ocean to the atmosphere above. Weaker winds in the Greenland Sea produces weaker flow and hence a larger sea ice extent and thickness.

Special Section:
Forum for Arctic Modeling and Observational Synthesis (FAMOS) 2: Beaufort Gyre phenomenon

Key Points:

- Stronger/weaker winds over the Greenland Sea result in stronger/weaker flow of Atlantic Water in the Nordic Seas and into the Arctic Ocean
- In the Barents Sea there is a linear relationship between Atlantic Water volume and heat transport, surface heat loss, and sea ice extent
- There is potential for predictability of the Arctic-Atlantic circulation based on wind forcing anomalies and climate response functions

Supporting Information:

- Supporting Information S1
- Movie S1
- Movie S2
- Movie S3
- Movie S4
- Movie S5
- Movie S6

Correspondence to:
M. Muilwijk,
morven@uib.no

Citation:
Muilwijk, M., Ilicak, M., Cornish, S. B., Danilov, S., Gelderloos, R., Gerdes, R., et al. (2019). Arctic Ocean response to Greenland Sea wind anomalies in a suite of model simulations. *Journal of Geophysical Research: Oceans*, *124*, 6286–6322. https://doi.org/10.1029/2019JC015101

Received 26 FEB 2019
Accepted 28 JUL 2019
Accepted article online 4 AUG 2019
Published online 30 AUG 2019

1. Introduction

Changes in climate associated with global warming are particularly pronounced at high northern latitudes. Over the past decades the Arctic has warmed twice as fast as the global mean (IPCC, 2014), a characteristic often termed “polar amplification” (Screen & Simmonds, 2010; Serreze & Barry, 2011). This Arctic warming manifests in many ways, for example, a dramatic and unprecedented decrease in sea ice extent (Carmack et al., 2015; Onarheim et al., 2018) and volume (Kwok, 2018). Since satellite observations began in the late 1970s, the Arctic summer sea ice extent has declined by approximately 50% (Vihma, 2014), and winter sea ice extent has steadily declined of 2.6% per decade (Cavalieri & Parkinson, 2012). Sea ice decline is projected to continue in the future, and these changes will alter Arctic ecosystems and fisheries (Dalpadado et al., 2014), influence transportation and exploitation of other natural resources (ACIA-Arctic Climate Impact Assessment, 2005), change the cycling of carbon (Hinzman et al., 2013), decrease the surface albedo Curry et al. (1995), and possibly affect climate and weather at lower latitudes (Liptak & Strong, 2014; Sorokina et al., 2016). For example, the decline of winter sea ice cover could increase the probability of cold winters in Europe (Cohen et al., 2014; Yang & Christensen, 2012).

Atmospheric forcing may be the biggest contributor to the sea ice loss (Serreze et al., 2007), but ocean heat storage and transport play an important role in certain regions (Carmack et al., 2015; Perovich & Richter-Menge, 2015; Polyakov et al., 2017). For example, the decline and variability in winter sea ice cover north of Svalbard and in the Barents and Kara Seas is linked to an increased and warmer inflow of Atlantic Water (AW; Årthun et al., 2012, 2017; Barton et al., 2018; Li et al., 2017; Onarheim et al., 2014, 2015, 2018). The Barents Sea experiences the fastest surface warming in the Arctic (Screen & Simmonds, 2010), and a recent study by Lind et al. (2018) found that the northern Barents Sea has transitioned from a cold Arctic to a warm Atlantic-dominated regime. It is expected that warming will continue, and projections from Onarheim and Arthun (2017) show that this region might become winter ice free in the time period 2061–2088 if the Representative Concentration Pathway scenario 8.5 (Moss et al., 2010) is followed. Although the recent Arctic surface changes have been well documented, the relative importance of the ocean remains uncertain and may increase in the future (Carmack et al., 2015). The observed trends in sea ice cover, atmospheric temperatures, and ocean heat transport due to increasing levels of greenhouse gases are superimposed on internal and natural variability. It is therefore of great interest to understand these current changes with respect to past change and to disentangle the different forcing factors in order to make skillful predictions for the future.

Variability in the Barents Sea sea ice extent has been attributed to a number of processes, and variations in the ocean heat transport is key (Årthun et al., 2012; Li et al., 2017; Smedsrud et al., 2013; Venegas & Mysak, 2000; Zhang, 2015). These heat anomalies result from either increased volume transport in the Norwegian Atlantic Current, a poleward extension of the North Atlantic Current (Muilwijk et al., 2018; Smedsrud et al., 2013), or temperature anomalies that are either generated locally (Schlichtholz & Houssais, 2011) or advected in from the south (Årthun & Eldevik, 2016; Furevik, 2001; Holliday et al., 2008; Skagseth et al., 2008). This has motivated several studies that have explored the effect of wind forcing on the AW volume and heat transport. Some studies focused on the impact of local wind forcing (Ingvaldsen et al., 2004; Lien et al., 2013, 2017; Skagseth et al., 2011), while others have described the influence of large-scale atmospheric forcing in terms of the North Atlantic Oscillation (NAO; Hurrell, 1995)—the dominant Northern Hemisphere (NH) mode of atmospheric variability (Dickson et al., 2000; Grotefendt et al., 1998; Orvik & Skagseth, 2003; Visbeck et al., 1998). As an example, Muilwijk et al. (2018) found a high correlation between the wind stress curl over the Nordic Seas and the ocean heat transport entering the Barents Sea.

Here, we further investigate the relationship between anomalous wind forcing, poleward ocean heat transport, and sea ice extent, with a particular focus on the Nordic, Barents, and Kara Seas using nine different climate and ocean sea ice-coupled general circulation models. Ocean sea ice-coupled general circulation models have been compared within the CORE2 project (Ilicak et al., 2016; Wang et al., 2016a, 2016b), and analyzed and improved during the last decades through the Arctic Ocean Model Intercomparison Project and its continuation, the Forum for Arctic Modeling and Observational Synthesis (https://famosarctic.com). Within this framework Marshall et al. (2017) proposed a coordinated modeling experiment with the goal to compute “climate response functions” (CRFs), the transient response of ocean and sea ice to abrupt “step” changes in external forcing fields. Here, we analyze how a suite of models respond to a step change in the Greenland Sea (GS) wind field (Figure 1), following the proposed protocol described in Marshall et al. (2017). We are motivated by three questions:

1. How does the general circulation of the Nordic Seas and poleward ocean heat transport into the Arctic Ocean respond to anomalous wind forcing over the GS?

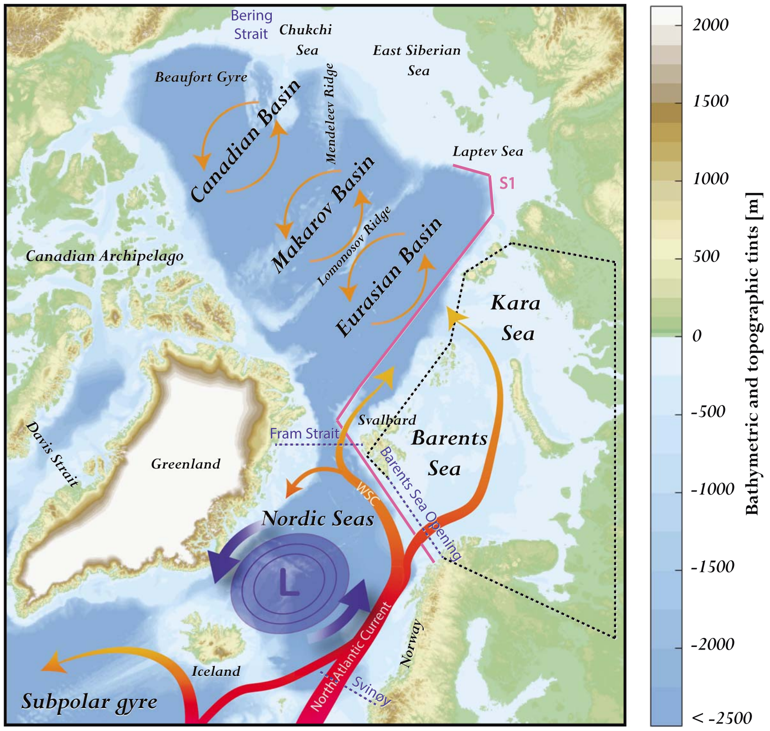

Figure 1. Overview map of the Arctic Ocean and its regional seas including the Atlantic Water inflow illustrated by the large red arrow. The blue arrows and low-pressure system illustrate the location of the Greenland Sea wind anomalies with stronger winds for the Greenland Sea Plus experiment and weaker winds for Greenland Sea Minus experiment. Orange arrows in the deep Arctic basins illustrate the circulation of intermediate Atlantic Water masses based on Carmack et al. (2015). Section S1 (presented in Figure S5) is shown in magenta, and the black dotted lines define the Barents and Kara Seas region.

2. What are the downstream effects of anomalous GS wind forcing on the deep Arctic Ocean basins and the Beaufort Gyre?
3. Does the system have any predictability?

Simulating the Arctic Ocean realistically is challenging due to the complexity of the dynamic and thermodynamic processes shaping its domain, in combination with the sparseness of long-term observations (Ilicak et al., 2016). Previous modeling studies document large differences in the mean state Arctic hydrography and AW inflow in different Arctic Ocean Model Intercomparison Project models (Holloway et al., 2007; Karcher et al., 2007) and Coupled Model Intercomparison Project models (Ilicak et al., 2016; Wang et al., 2016a, 2016b). The uniqueness and strength of the CRFs is that we study the model responses to external forcing rather than comparing their mean states. This allows us to focus on the forcing mechanism physics, similar to what is done in idealized studies such as Lique et al. (2015). A CRF approach also allows determination of time scales on which the system adjusts to changing forcing, which helps to understand the dynamical balance and predictability of the system. Here, step functions are useful because one can, if assuming linearity, reconstruct the response to any historical forcing based on the impulse response from the step function (Marshall et al., 2017). The ultimate goal is thus to learn how the Arctic Ocean responds to changes in external forcing. The differences and similarities across model responses give insights into the robustness of the results and the memory of the system.

The paper is organized as follows. A description of the region and a summary of previous studies investigating the relationship between wind forcing, ocean heat, and sea ice is given in section 2. The models and experimental setup are briefly described in section 3. In section 4 we explain the different responses to our perturbation experiment and investigate the potential for prediction based on a convolution of the CRFs with observed wind forcing. In section 5 we provide some further discussion on model differences and the redistribution of AW heat. We summarize our conclusions in section 6.

2. Background

Enclosed by the Eurasian and North American landmasses, the Arctic Ocean is the smallest of the world's five (major) oceans. The Arctic Basin has three subbasins deeper than 2,500 m: the Eurasian, Makarov, and Canadian Basins. These are separated by two ridges: the Lomonosov Ridge and the Mendeleev Ridge (Figure 1). Surrounding these deep basins are extensive continental shelf areas (≤500 m) that cover a third of the total area: the Chukchi, the East Siberian, the Laptev, the Kara, and the Barents Seas. The Arctic Ocean is connected to the Pacific through the Bering Strait. We define the Nordic Seas—the Greenland, Iceland and Norwegian Seas—to be included in the Arctic Ocean, that is, in what Aagaard et al. (1985) termed the Arctic Mediterranean. This Arctic Ocean definition follows that of the International Hydrographic Office (Jakobsson & Macnab, 2006). The Fram Strait (FS) and the Barents Sea Opening (BSO) connect the deep Arctic basins with the Nordic Seas, while the Canadian Archipelago connects Arctic waters to the Labrador Sea through Baffin Bay. Most of the Arctic Ocean is characterized by a seasonally varying sea ice cover. With maximum extent in March and minimum extent in September, it influences ocean stratification, circulation, and freshwater and heat budgets (Haine et al., 2015).

2.1. AW Circulation and Atmospheric Forcing

AW that flows through the FS and the BSO is the dominant source of ocean heat and salt to the deep Arctic basins (Aagaard et al., 1987; Muilwijk et al., 2018). This AW current is an extension of the North Atlantic Current (Figure 1), which brings warm and saline water masses of subtropical origin into the Nordic Seas. In the Nordic Seas the AW flows in two main current branches, one that circulates and feeds the interior of the Nordic Seas, and one flowing northward as the Norwegian Atlantic Slope Current (Orvik et al., 2001; Wekerle et al., 2017). This current finally enters the BSO between Norway and Svalbard and enters the FS as the West Spitsbergen Current off the west coast of Svalbard (Beszczynska-Möller et al., 2012; Pérez-Hernández et al., 2019). A portion recirculates in FS (Hattermann et al., 2016; Wekerle et al., 2017), but the AW that does not circulates cyclonically in the Eurasian Basin, and a portion reaches the Makarov and Canadian basins, before it finally exits through the FS with the East Greenland Current or through the Canadian Archipelago (Carmack et al., 2015). The northward flow of AW in FS varies between 4 and 8 Sv (Beszczynska-Möller et al., 2012), while that in the BSO is close to 2 Sv (Smedsrud et al., 2010).

The NAO explains more than one third of the temporal variance in large-scale sea level pressure (SLP) in the North Atlantic. Its index is based on the difference between the subtropical (Azores) high and the subpolar low northeast of Iceland (Hurrell, 1995). Dickson et al. (2000) found that both the temperature and volume transport of AW to the Arctic Ocean increases during a strong positive NAO phase, which is characterized by an intense subpolar low and strong meridional pressure gradient. This strong pressure gradient results in stronger wind forcing in the North Atlantic, and thus an increased wind-driven northward AW current. The latter is supported by a comprehensive series of studies (Czaja & Marshall, 2001; Eden & Jung, 2001; Furevik, 2001; Langehaug et al., 2012; Lohmann et al., 2009; Medhaug et al., 2012; Muilwijk et al., 2018; Visbeck et al., 2013).

2.2. The Barents Sea and AW Impact on Sea Ice

The Barents Sea is a key region for determining the thermodynamic state of the Arctic Ocean. It dominates the region's heat storage, and more than 50% of the Arctic Ocean's surface heat loss occurs here (Serreze et al., 2007). In their pioneering work, Helland-Hansen and Nansen (1909) noted that varying inflow of AW influences the seasonal sea ice cover by determining the amount of winter freezing. This, and how the AW is modified before it exits the Barents Sea through the St. Anna Trough, has since been described by several other studies (Årthun & Schrum, 2010; Sandø et al., 2010; Smedsrud et al., 2010, 2013).

In the Arctic Basin, exchange from AW to the mixed layer and sea ice above is generally suppressed because of strong stratification (Carmack et al., 2015; Lind & Ingvaldsen, 2012; Lind et al., 2016). However, near the inflow regions such as the southern Barents Sea and north of Svalbard, where the AW layer is close to the surface or near steep topography, more of the heat reaches the surface and can contribute to direct bottom melting (Ivanov et al., 2016; Sandø et al., 2014). It has also been suggested that, with further warming of AW and increase of northward ocean heat transport, the warm AW might reach further into the Arctic Ocean. This so-called "Atlantification" represents an essential step toward a new Arctic climate state, with a substantially greater role for Atlantic inflow (Polyakov et al., 2017). As the sea ice becomes thinner, it is more mobile and less resistant to wind, surface, and tidal currents, facilitating the creation of more open-water areas. This may lead to a positive feedback. For example, increased input of momentum feeds turbulent

Table 1
Summary of the Models Participating in the Experiment in Alphabetical Order

Group	Ocean model	Ice model	Horiz. res.	Domain/grid	Forcing
Alberta	NEMO v3.4	LIM 2	Nominal 0.5°	Regional/ANHA2	2002–2016 CGRF (Smith et al., 2014)
AWI-MPI	MPIOM	MPIOM	Nominal 1.5°	Global/bipolar	Partially coupled, wind from NCEPcfsr (Saha et al., 2010)
FESOM	FESOM	FESIM	25km in Arctic	Global/bipolar	1948–2009 CORE-II (Griffies et al., 2012)
IFREMER	NEMO v3.6	LIM 3.5	Nominal 0.25°	Regional/CREG025	1979–2015 DFS 5.2 (Brodeau et al., 2010)
ITU-MOM	MOM5	SIS	Nominal 1°	Global/tripolar	1948–2009 CORE-II (Griffies et al., 2012)
JHU	MITgcm	MITgcm	Nominal 1/8°	Regional	ERA-Interim 1998 repeat year
MIT	MITgcm	MITgcm	36 km	Regional/cubedsphere	1979–2013 JRA-25 (Onogi et al., 2007)
NorESM	NorESM-O	CICE 4	Nominal 1°	Global/tripolar	1870–2009 20CR (He et al., 2016)
Ox-HiGEM	HiGEM	CICE 4	Nominal 1/3°	Global/bipolar	Fully coupled

mixing, which again could assist in bringing more AW heat to the surface (Peterson et al., 2017). Therefore, both the variation of the AW inflow and the local processes in the Barents Sea are important.

3. Experiment Setup for the Ocean-Only Models

In this coordinated study, the models considered have different resolutions, domains (both global and regional), and different atmospheric forcing (see Table 1). The common factor is that the models are perturbed by adding the exact same anomaly of wind/SLP to the original forcing. These wind anomalies affect all the forcing fields (and in particular the air-sea heat flux), which depend on the wind when estimated through a bulk formula. All other modeling choices are the preference of individual groups.

Prior to the sensitivity experiments, the models were run with an unperturbed atmospheric forcing covering a historical period. Several models use the CORE-II forcing (Griffies et al., 2012), but other reanalysis products are also used (Table 1). The perturbation experiment was then conducted by modifying the forcing field instantly after the models were “spun up” for a period of time (Marshall et al., 2017). Most perturbed runs were over the same time period (with the anomalous SLP field added in January 1980), and the difference between simulated fields in the perturbed and the control runs was used to evaluate the models responses. Exceptions are the Alberta model, which was run for the period 2002–2016 (and then repeated the 2002–2016 forcing to have a total of 30 model years like the other model runs), and the JHU setup, which uses repeat-year forcing.

The CRF of a certain diagnostic (e.g., the barotropic stream function, AW volume transport, or sea ice extent) was calculated as the difference between the perturbed and control simulation. The evaluation of step function anomalies and responses is used to distinguish between linear and nonlinear responses in the climate system (Gregory et al., 2015). From the CRFs, it is possible to construct the linear response to time history of the forcing (Marshall et al., 2014). One may calculate the evolution of the variable $R(t)$ by (see, e.g., Marshall et al., 2014)

$$R(t) = \int_0^t CRF(t-t')\frac{\partial F}{\partial t}(t')dt', \tag{1}$$

where F is the anomalous forcing (wind anomaly in the present study) and $CRF(t)$ is the time-dependent response to a unit step change in forcing.

3.1. Description of Models

We analyze monthly mean output from nine different models, five of which are global in extent. Key details of model configurations are given in Tables 1 and 2. The IFREMER and Alberta groups both use a regional model based on the Nucleus for European Modelling of the Ocean (Madec, 2014), but with different versions and resolution. The IFREMER version is a regional extraction (i.e., the “northfold” discontinuity of the global grid is removed) of the ORCA025 configuration, and the Alberta group uses a regional extraction of the ORCA05 configuration, both developed jointly by the Drakkar consortium and Mercator-Ocean (Barnier et al., 2009), encompassing the Arctic and parts of the North Atlantic down to 20° S. The Alberta

Table 2
Detailed Information About the Participating Models

Group	Vertical	Tracers	Background vertical diffusivity	Runoff
Alberta	z (50)	No	TKE model (Blanke & Delecluse, 1993)	Bamber et al. (2012), Dai and Trenberth (2002), (Dai et al., 2009)
AWI-MPI	z (40)	No	(Pacanowski & Philander, 1981) scheme	Coupled MPI-ESM
FESOM	z (47)	Yes	KPP scheme (Wang et al., 2014)	Dai and Trenberth (2002), Dai et al. (2009)
IFREMER	z (75)	no	TKE model (Blanke & Delecluse, 1993)	Bamber et al. (2012), Dai and Trenberth (2002), Dai et al. (2009)
ITU-MOM	z (50)	Yes	KPP scheme (Dunne et al., 2012)	Dai and Trenberth (2002), Dai et al. (2009)
JHU	z (50)	No	KPP scheme (Wang et al., 2014)	AOMIP
MIT	z (50)	Yes	KPP scheme (Wang et al., 2014)	Dai and Trenberth (2002), Dai et al. (2009)
NorESM	σ_2 (52)	Yes	TKE model (Fox-Kemper et al., 2008)	Dai and Trenberth (2002), Dai et al. (2009)
Ox-HiGEM	z (40)	No	Hybrid scheme (Shaffrey et al., 2009)	n/a

configuration has 50 geopotential levels in the vertical, and climatological conditions are provided by GLORYS2v3 (Masina et al., 2015). The IFREMER configuration has 75 geopotential levels and uses the initial conditions from World Ocean Atlas 2009 (Levitus et al., 2009).

The MITgcm is another regional Arctic Ocean simulation (Marshall et al., 1997) with a setup as described in Marshall et al. (2017). JHU (Stewart & Haine, 2013) is also a regional MITgcm configuration but uses 1998 repeat-year surface forcing and idealized open boundary conditions.

Of the five global models participating, the ocean component of the Norwegian Earth System Model (Bentsen et al., 2013) from the Bergen working group is the only model that has isopycnic layers (52 in number) in the vertical. For an in-depth analysis of physical mechanisms, a 120-year-long control simulation is used from NorESM, which is forced by a twentieth century reanalysis product. The setup of this model is similar to He et al. (2016), and an evaluation of the AW variability was performed by Muilwijk et al. (2018).

The only unstructured-mesh model in the analysis is FESOM Version 1.4 (Wang et al., 2014), a community ocean ice model developed and maintained by the Alfred Wegener Institute (AWI). FESOM is a global multiresolution ocean general circulation model using triangular meshes (Danilov et al., 2004; Wang et al., 2008). Its sea ice component is also formulated on the same surface triangular meshes (Danilov et al., 2015). In this study we employed a global setup at a nominal 1° horizontal resolution in most parts of the ocean and 24-km resolution north of 45° N. The resolution is refined along the coast and in the equatorial band. In the vertical, it has 47 z levels with 10-m resolution in the upper 100-m depth. This setup has been used in several previous studies with a focus on the Arctic Ocean (Wang et al., 2016a, 2016b, 2019).

The AWI-MPI group uses the fully coupled atmosphere-ocean-sea-ice-model MPI-ESM. A detailed description of the ocean component of the model can be found in Jungclaus et al. (2013). Wind anomalies are applied following the so-called Modini method, a partial coupling approach of Thoma et al. (2015). This method enables the ocean component of MPI-ESM to be driven by prescribed wind forcing, while maintaining consistency of heat and energy exchanges between the atmosphere and the ocean, and allowing feedbacks between climate system components.

The ocean component of the ITU-MOM uses the Modular Ocean Model (MOM5) code from Griffies (2012). MOM5 employs an Arakawa B-grid with nominal 1° horizontal grid resolution and bathymetry (refined meridionally to 1/3 degree at the equator) and a tripolar grid poleward of 65° N. The vertical grid has 50 levels, with 22 in the upper 220 m. This grid configuration was also used in the CORE-II intercomparison experiments (Danabasoglu et al., 2014; Farneti et al., 2015; Griffies et al., 2014). K-Profile (Large et al., 1994) and GM (Gent & Mcwilliams, 1990) parameterizations are used for vertical and isoneutral mixing, respectively. Further details of the numerical methods and physical parameterizations of the ocean are provided in Dunne et al. (2012).

Finally, we also analyze results from the Ox-HiGEM group with the fully coupled HiGEM climate model (Shaffrey et al., 2009). This model is not perturbed using the same approach as the forced simulations, but instead, multiple linear lagged regression is used to extract the responses to a hypothetical step increase in the principal components of Greenland Sea Plus (GSP) SLP pattern. This method is described by Kostov et al. (2017) and in section 3.3.

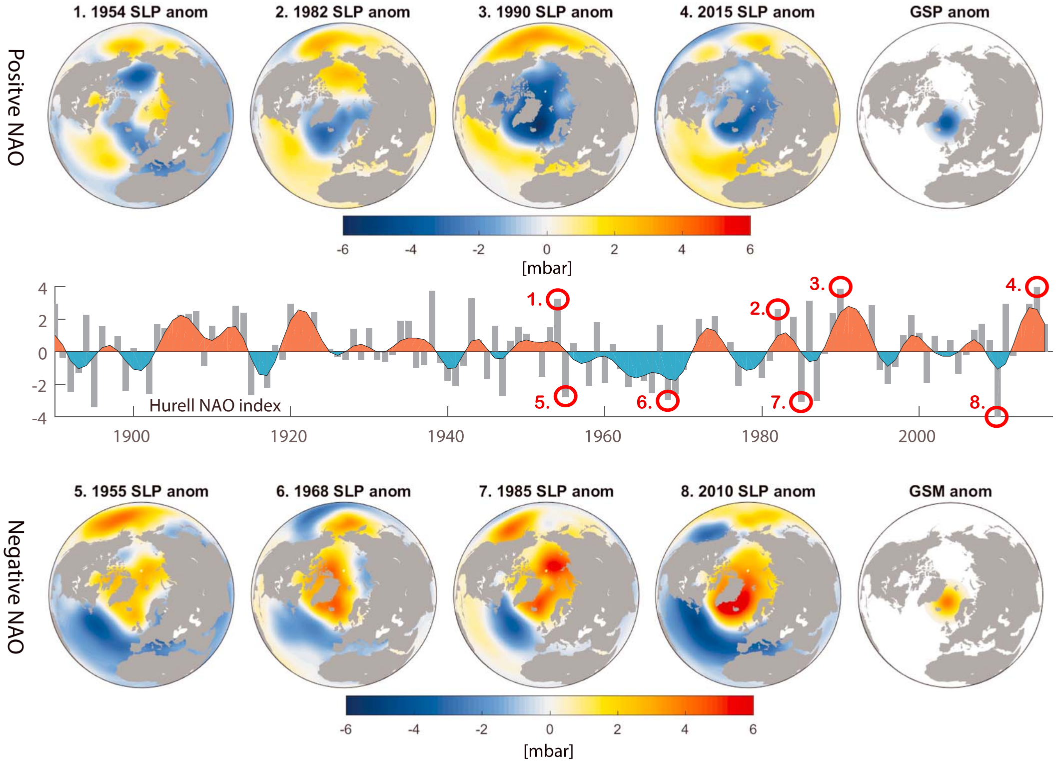

Figure 2. North Atlantic sea level pressure (SLP) anomalies over time. In the middle is the Hurell North Atlantic Oscillation (NAO) index with observed temporal variability. Maps of SLP anomalies for selected years with a strong positive NAO phase (1–4) are shown above, and selected years with a strong negative NAO phase (5–8) are plotted below. For comparison, the idealized SLP perturbation anomalies used for the Greenland Sea Plus (GSP) and Greenland Sea Minus (GSM) experiments are shown on the right. Note the GSP corresponds to anomalously low pressure over the Greenland Sea (stronger wind forcing) and GSM corresponds to anomalously high pressure (weaker wind forcing).

3.2. Wind Anomalies

The perturbation experiments consist of anomalous low/high SLP in the GS region, hereafter called the GSP/Greenland Sea Minus (GSM) experiments. GSP results in a stronger mean cyclonic atmospheric circulation, and GSM results in a weaker mean cyclonic atmospheric circulation. The anomalous pressure fields are shown in Figure 2. The center of the anomalies are located in the Greenland Sea at 70.55° N and 6.04° W (Figure 2) and have a magnitude of 4 mbar with a radius of influence of approximately 1,000 km. Compared to seasonal changes in SLP, reaching 20–30 mbar, the applied anomalies are relatively weak. The anomalous forcing is of the same order of magnitude as the long-term trends in the Arctic (Marshall et al., 2017), and comparable locally in the GS to the difference between a NAO neutral year and a strong positive/negative NAO year (Figure 2). The anomaly is located near the northern center of action of the NAO and is also termed the Icelandic Low. We use the term GS low from now on.

The center of this anomaly is similar to the first empirical orthogonal function of SLP in Thompson and Wallace (1998), who described the NAO as a regional manifestation of a hemispheric mode of variability that they named the Arctic Oscillation. The GS low is likely to be dominant during winter (Hurrell, 1995), and the anomaly center has shifted northeastward in recent decades (Moore et al., 2013; Zhang et al., 2008). Studies have shown that another center of SLP variability can be found in the Nordic Seas, named the Lofoten Low (Jahnke-Bornemann & Brümmer, 2009; Moore et al., 2012). Therefore, a perturbation experiment similar to our GS SLP perturbation was performed using the MIT model with the center of the anomaly shifted toward the Lofoten Low. Results from this experiment showed that the responses of the AW circulation were very similar to those in the GS perturbation experiment (not shown). Hence, we conclude that the GS anomaly is well located for our investigation of responses.

3.3. CRFs From the Fully Coupled HiGEM Simulation

The Ox-HiGEM CRFs are calculated from the coupled climate model HiGEM. The method, following Kostov et al. (2017), first identifies a target time series and a forcing time series, the latter of which is thought to exert some control on the former. The target time series is one of the metrics under investigation and is deseasonalized; the forcing time series is the regression of deseasonalized SLP variability onto the prescribed GSP anomaly pattern. The target time series is then considered as a convolution of the forcing time series with an unknown impulse response function. A solution for the impulse response function is found using multiple linear least squares regression of the target against the lagged forcing. Thousands of estimates are obtained for the impulse response function by varying (a) the cutoff lag, between 30 and 35 years; (b) the part; and (c) the length of the control run of the regression. The mean of these estimates for the impulses over the first 30 years is taken. Because this technique relies on a linear method, the symmetrical GSP and GSM forcing anomalies yield symmetrical responses. An estimate of uncertainty is derived from combining, in quadrature, the standard deviation of all estimates with a measure of the error associated with the fit between the original target and a convolution of each impulse estimate and the forcing, shown in Figure S8 in the supporting information. Finally, a step response is obtained by integrating the impulse response through time lags. The same technique was employed by Johnson et al. (2018) to probe the time-evolving relationship between Arctic freshwater and atmospheric circulation in HiGEM. This method is only used for the Ox-HiGEM CRFs.

3.4. Tracer Release

Passive tracers have been released “online” in four of the participating models (FESOM, ITU, MIT, and NorESM) in order to track the AW transport routes both in the climatology and perturbation experiments. The usage of “online” passive tracers in ocean circulation models is a useful method to investigate advection pathways and diffusion of water masses. One can view the tracers as a conservative dye that colors water particles with a certain concentration. At the release point the tracer concentration is set to 100% for every integration time step, starting in January 1980. It is then advected and diffused as the water masses circulate and mix. The passive tracers have been released in three locations along the AW flow (Figure 1): in the North Atlantic Current at the Svinøy section (63° N), in the BSO (70–74° N), and in the FS (79° N). Tracer diagnostics are computed as depth-integrated tracer volume for each grid cell.

4. Results

4.1. Circulation of AW in the Nordic Seas and Response to Wind Perturbations

In this section, the circulation of AW in the Nordic Seas and its relationship to the overlying atmospheric forcing is examined, followed by the responses of the AW flow to the two wind perturbation experiments, GSP and GSM.

In order to quantify the strength of the AW circulation in the Nordic Seas, an integrated quantity, like a “gyre index,” is useful. To this end, the spatial pattern of the annual mean sea surface height (SSH) and the barotropic stream function have been examined using empirical orthogonal function analysis of the 120-year-long NorESM control simulation (Muilwijk et al., 2018). The barotropic stream function is here defined as

$$\psi = -\int_{\text{east}}^{\text{west}} v dx, \quad u = \frac{-\partial \psi}{\partial y} \quad \& \quad v = \frac{\partial \psi}{\partial x}, \tag{2}$$

where u and v are the depth-integrated currents in the x and y directions. As previously shown by Aagaard (1970), Nøst and Isachsen (2003), and Chatterjee et al. (2018), the leading mode features a barotropic cyclonic circulation in the Nordic Seas. Consequently, the area-average barotropic stream function over the central Nordic Seas (bounded by 66–76° N, 15° W to 10° E) can be used as an indicator of the strength of the Nordic Seas gyre circulation. A time series of the monthly mean NorESM barotropic stream function for the period 1880–2009 is shown in Figure S1. This time series shows that the NorESM barotropic circulation has a mean strength of approximately 6 Sv. Seasonally, it varies with a range of approximately 7 Sv, and interannual variations are approximately 1–3 Sv. Significant (with 95% confidence) positive correlations ($\bar{r} = 0.7$) are found between the area-averaged barotropic stream function and the wind stress curl in both the Nordic

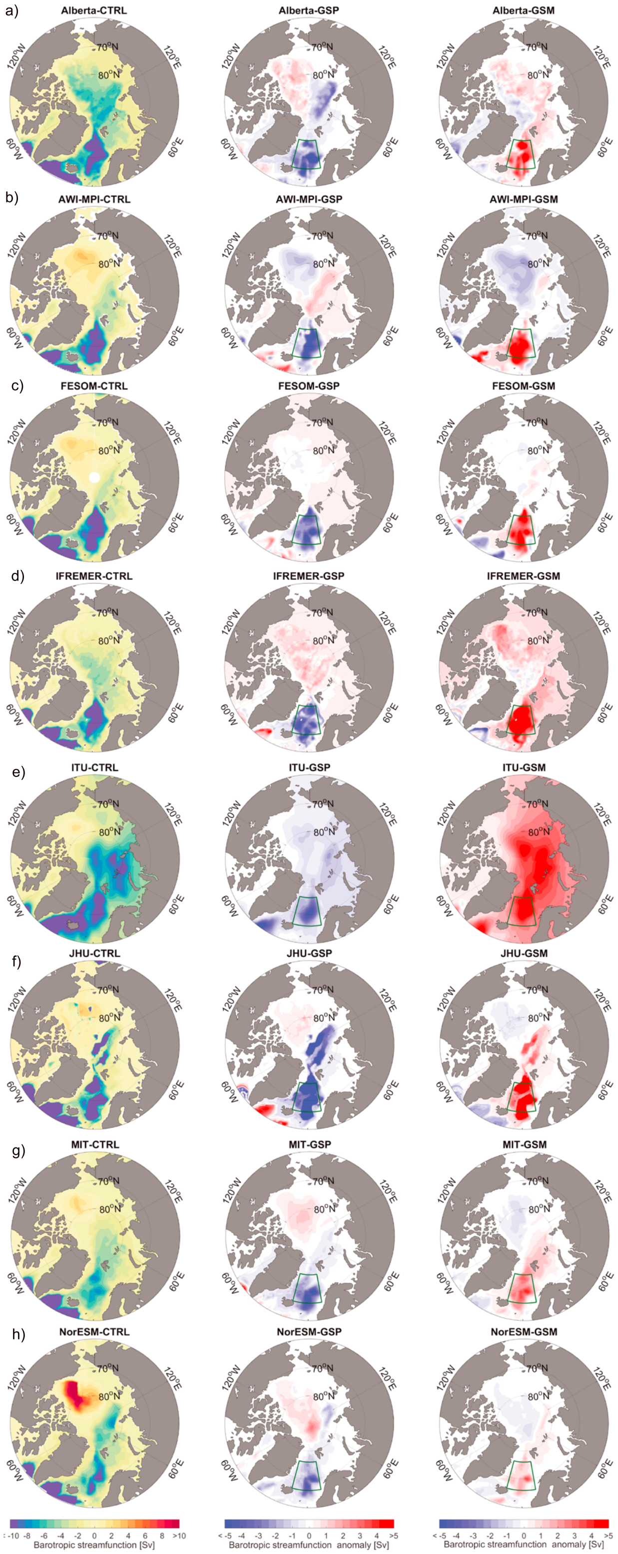

Figure 3. Annual mean barotropic stream function computed from each of the models. Negative values denote cyclonic circulation, and positive values denote anticyclonic circulation. Panels on the left show the control simulations. Middle panels show anomalies resulting from the Greenland Sea Plus (GSP) experiment (stronger wind forcing), and right panels show anomalies resulting from the Greenland Sea Minus (GSM) experiment (weaker wind forcing). All values are averaged over the last 10 years of integration (20–30 years after perturbation).

Seas and the Subpolar Gyre, and the NAO index (Figure S1c). Throughout the remainder of the text, all statistical significance has been determined using a Student's *t*-test.

4.1.1. Mean State

On average, all models have a similar spatial pattern in the Nordic Seas, a cyclonic ocean circulation that is strongest in the GS and Lofoten Basin (Figure 3). The cyclonic flow starts at the Greenland-Scotland Ridge and extends all the way north to FS in all models. This is due to a low in the SSH field in the central Nordic Seas caused by Ekman divergence as presented for NorESM in Figure 5a.

The absolute magnitude of the barotropic stream function generally varies between −8 and −10 Sv in the Nordic Seas (Figure S1c). An exception is the JHU model where the barotropic stream function is five times stronger than the other models. This has been investigated further and appears to be connected to strong deep circulation in the deep parts of the basins. Figure 3 clearly displays differences in the spatial pattern of the cyclonic flow between the models. Some models have a strong circulation throughout the entire Nordic Seas, while others are more confined to the smaller basins. Based on Nøst and Isachsen (2003), these differences are possibly linked to variations in Ekman pumping, the local bathymetry and its discrete representation, and the parameterization of the eddy field based on the actual hydrographic background states. The latter also results in different geostrophic currents. We will further explore these issues in section 5.1.

In the other Arctic basins the strength of the flow is less consistent between models (Figure 3), which could indicate different circulation patterns among the models. Further north, most models show a relatively strong cyclonic circulation in the Eurasian Basin, indicating that most of the AW recirculates here. A part of the AW continues to circumnavigate the Arctic Basin as a boundary current. As is shown by passive tracers in section 5.3, models differ by how the AW crosses the Lomonosov Ridge and extends into the Canadian Basin. The Alberta and ITU-MOM models have relatively strong cyclonic circulation throughout most of the Arctic Basin. An anticyclonic barotropic stream function is observed in the Beaufort Gyre for the AWI-MPI, FESOM, ITU-MOM, JHU, MIT, and NorESM models, but its magnitude and spatial pattern vary considerably. In the Beaufort Gyre the cyclonic circulation in the AW layer sits beneath the anticyclonic surface layer, so differences in the barotropic stream function, which integrates the two, may be a product of different halocline depths between models (Steiner et al., 2004). In the Beaufort Gyre, differences in the circulation may also be due to differences in vertical mixing (Zhang & Steele, 2007) or the simulated sea ice cover (not shown), as explained by the "ice-ocean governor" theory of Meneghello et al. (2018) and Wang et al. (2019). They argue that when wind blows over the ice, the ice drags the ocean, but when the gyre spins up, the geostrophic current catches up with the ice, and the surface stress is reduced. To first order, if simulated sea ice states are different among the models, the momentum transfer from the air to the ocean will also be different. Due to the lack of ocean current observations in the Arctic Ocean, the real barotropic stream function is not well known. We can therefore only compare the models with each other.

4.1.2. Response to Perturbations

Stronger cyclonic atmospheric wind forcing in the GSP enhances the Ekman divergence, leading to a deepening of the SSH trough in the Nordic Seas, as is seen for NorESM in the middle panel of Figure 4a. The perturbation also causes a stronger SSH gradient between the Arctic Basin and the Nordic Seas, which results in an increased barotropic flow as is seen in the center panels of Figure 3. All models behave consistently in this respect, and the average response is a 50% increase of the average barotropic stream function in the Nordic Seas. The JHU barotropic response is approximately five times stronger than that for the other models. All models show a slightly weaker, and in some cases opposite, response in the Eurasian Basin. We note that a local wind anomaly in the GS sets up a barotropic response extending over the entire Arctic Ocean, consistent with Peralta-Ferriz et al. (2014), and also upstream into the Subpolar Gyre (Figure S4) for most models. The weakened cyclonic atmospheric wind forcing in the GSM experiments results in a nearly identical, but opposite, response. This is consistent with previous analyses based on observations (Curry & McCartney, 2001) and model simulations (Brauch & Gerdes, 2005).

The spatially averaged barotropic stream function anomalies in the Nordic Seas governed by the GSP and GSM experiments are shown in Figure 5a. The amplitude of the response varies between 2–4 Sv in the GSP case and 1–5 Sv in the GSM case. Some asymmetry is seen among the responses, with the strongest response and largest spread for GSM. It also appears that the variability in the GSM case is larger than in the GSP case and that the ITU-MOM and IFREMER models do not reach equilibrium after 30 years. Ox-HiGEM has the weakest response for both cases, but this response increases over time. NorESM has

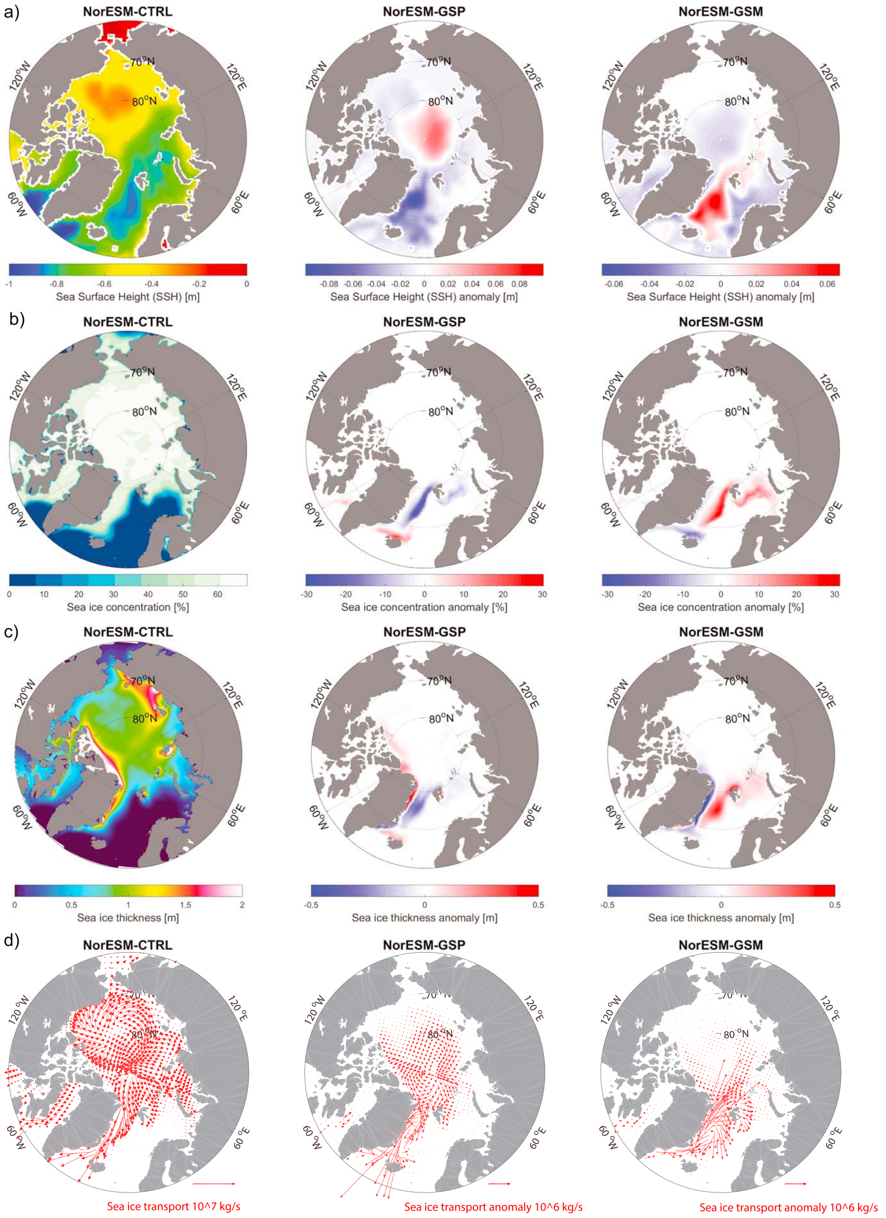

Figure 4. Annual mean and mean response for sea ice and SSH) in the NorESM model due to wind forcing. Panels on the left show the control simulation, middle panels show anomalies resulting from the stronger GSP forcing, and right panels show anomalies from the weaker Greenland Sea Minus (GSM) forcing. All values are averaged over the last 10 years of integration (20–30 years after perturbation). (a) SSH, (b) sea ice concentration, (c) sea ice thickness, and (d) sea ice transport. GSP = Greenland Sea Plus.

the lowest response of the models without an atmosphere, but otherwise, these are relatively similar. The response began in 1980 for most models, with a typical 2- to 5-year dynamic adjustment time before a new quasi-equilibrium state was obtained, in qualitative agreement with the findings in He et al. (2016). We find that the barotropic response to the wind anomalies is immediate and happens in the first month. This is also why the largest response is seen in the first year. The adjustment time scale is mainly set by dynamical adjustment of temperature and salinity. For NorESM this is investigated by looking at the depth-evolution of isopycnal layers (Figure S10). The perturbation results in a slow uplifting of the isopycnals, and the response in the intermediate and deep layers is therefore delayed by some years. A part of this delayed response might be advective, but it might also be related to convective mixing. This is discussed further in the upcoming sections.

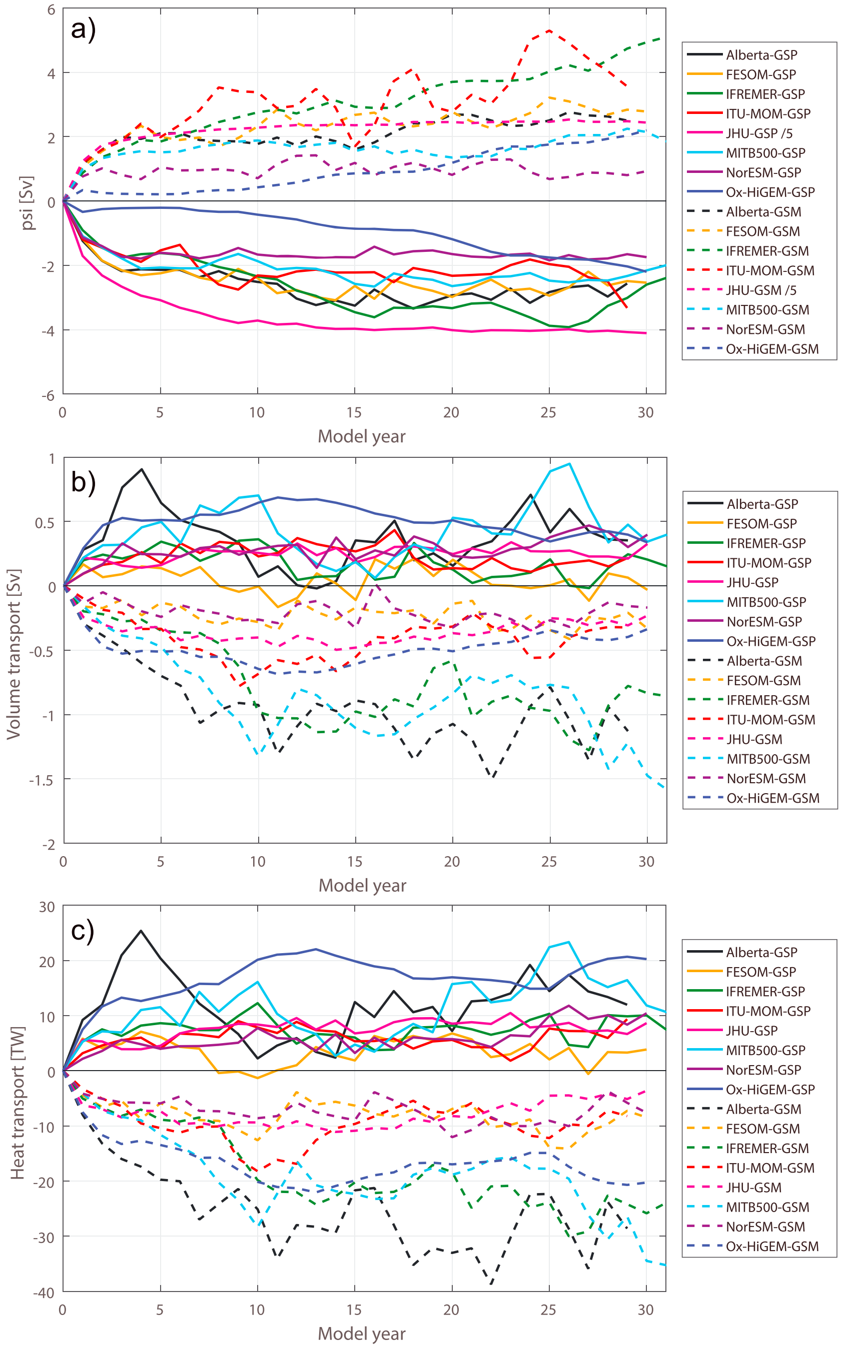

Figure 5. Annual mean Nordic Seas and Barents Sea climate response functions for the Greenland Sea Plus (GSP) and Greenland Sea Minus (GSM) wind anomalies. (a) Nordic Seas barotropic stream function strength (negative GSP values indicate stronger cyclonic circulation), (b) Barents Sea Opening inflow volume, and (c) Barents Sea Opening heat transport. The 4-mbar GSP and GSM forcing is shown in Figure 2, and the Nordic Seas area in Figure 3. The JHU response in (a) has been divided by 5 to scale with the other models.

4.2. Volume and Heat Transport Through the BSO

Ocean heat transport varies due to changes in both temperature and volume, and its absolute value depends on the chosen reference temperature (Schauer, 2004). We have chosen 0 ° C as a reference temperature for the inflow. Årthun et al. (2012) and Schauer et al. (2002) showed that 0 ° C is a representative value for the cold waters exiting the Barents Sea to the deep Arctic Basin, and we therefore simplify and refer to this transport as a heat transport and not a temperature transport. We acknowledge, however, that a physically consistent

Table 3
Climatological Values Obtained From the Control Simulations of the Different Models

Group	Barotropic stream function Nordic Seas (Sv)	Inflow volume transport BSO (Sv)	Inflow heat transport BSO (TW)	Sea ice extent Barent and Kara Seas (10^{11} m^2)	Sea ice extent NH (10^{12} m^2)	Net surface heat flux Barents and Kara Seas [TW]
Alberta	−8.0 (0.7)	+4.3 (0.5)	+100.2 (15.8)	+10.0 (1.7)	+10.4 (0.3)	-82.1 (21.7)
AWI-MPI	−8.8 (0.7)	+3.5 (0.3)	+99.2 (8.3)	+11.1 (0.9)	+11.1 (0.2)	-109.0 (13.3)
FESOM	−7.7 (0.8)	+3.4 (0.3)	+68.4 (8.8)	+11.7 (1.1)	+12.9 (0.3)	-82.3 (10.0)
IFREMER	−4.8 (1.1)	+2.8 (0.3)	+53.4 (7.6)	+13.6 (1.1)	+11.5 (0.2)	-71.9 (10.1)
ITU-MOM	−7.9 (1.1)	+2.2 (0.4)	+38.9 (8.6)	+13.8 (1.5)	+12.0 (0.4)	-55.0 (10.1)
JHU	−32.0 (0.0)	+3.6 (0.0)	+67.6 (0.0)	+16.9 (0.0)	+12.3 (0.0)	-32.6 (0.0)
MIT	−5.9 (0.7)	+3.3 (0.4)	+58.8 (11.7)	+13.5 (1.2)	+12.1 (0.3)	-42.0 (13.9)
NorESM	−6.5 (1.0)	+2.9 (0.3)	+51.7 (7.8)	+13.6 (1.0)	+12.0 (0.3)	-73.1 (10.1)
Ox-HiGEM	−7.9 (1.8)	3.4 (0.8)	+93.6 (18.7)	+9.1 (1.3)	+8.7 (0.3)	-254.7 (40.3)

Note. Values represent annual means averaged over the time period 1980–2005, with the exception of the Alberta model, which covers the period 2002–2016, and the JHU model, which utilizes a 1998 repeat year. We note that observational values also do not cover the exact same time period as the model averages. The observed value of the net surface heat flux only covers the Barents Sea and not the combined Barents and Kara Seas. Values in parenthesis are the standard deviations (annual cycle not included).

ocean heat budget independent of reference temperature results only from the heat convergence of a closed mass budget (Montgomery, 1974; Schauer & Beszczynska-Möller, 2009). To calculate such a closed heat budget for the Barents and Kara Sea region would require calculating the $V'T'$ terms on very short time scales at all grid points. This diagnostic was regrettably not available for all the models.

Temperature fluctuations are important for the BSO heat transport, but it is dominated by volume fluctuations (Muilwijk et al., 2018; Smedsrud et al., 2013). The CRFs of the associated heat transports are calculated relative to 0 ° C, and overall, there is consistent CRF response among the models for the eastward volume and heat transport (Figure 5). There is some interannual variability in the CRFs, and it is still an ongoing research project to fully understand this, but we believe that this variability is a nonlinear response to the daily forcing of the models. Volume and heat transport through the BSO in the AWI-MPI model show interannual variability that is much larger than the response to the forcing anomalies. Therefore, the response cannot be clearly identified. As a consequence, responses further downstream in the Arctic are also obscured by large variability. The AWI-MPI model results concerning the BSO fluxes and Arctic metrics are therefore excluded from the following analysis and are shown instead in Figure S9.

In the case of GSP, models show an increased flow of AW into the Barents Sea (Figure 5b). On average, the GSP response is +0.3 Sv, resulting in an advected heat anomaly of approximately 7 TW. For comparison, the multimodel mean volume and heat transports are 3.3 Sv and 62 TW, respectively. Thus, GSP results in roughly 10% increase in the transports. The multimodel mean is slightly elevated compared to observations indicating 2.3 Sv of total inflow in the BSO (Smedsrud et al., 2013). However, because observations are only available for AW inflow since 1998, there are substantial uncertainties in variations in the strength and extent of the Norwegian Coastal Current, and there are no observations available between Bear Island and Svalbard where models indicate a small net inflow. The simulated multimodel mean heat transport is smaller than the observation-based estimate of 70 TW (Smedsrud et al., 2013), with only one model exceeding the observation-based value (Alberta; 100 TW; Table 3). This implies that in most models water flowing east in the BSO is too cold.

There is a connection between the barotropic circulation anomalies in the Nordic Seas (Figure 5a) and the BSO volume transport anomalies (Figure 5b). A strong Nordic Seas cyclonic circulation due to GSP, resulting in negative stream function anomalies, occurs simultaneously to a stronger BSO inflow. However, the BSO transport anomalies are more variable and have a wider spread. Also, one model (FESOM) crosses the zero line several years after the initial response. There may be several reasons for these large differences among the models. First, the branching of the North Atlantic Current (between the BSO, FS, and recirculation near the FS) and the connection between the AW flow in the Nordic Seas and the BSO transport appear

	Alberta	FESOM	IFREMER	ITU	MITB500	NorESM
Psi & BSO volume	n.s.	n.s.	0.59	0.57	0.65	0.42
Psi & FS volume	n.s.	n.s.	n.s.	n.s.	n.s.	0.34
BSO volume & BSO heat	0.97	0.94	0.93	0.92	0.95	0.91
BSO heat & SI extent	n.s.	n.s.	n.s.	0.38	n.s.	0.49
BSO heat & SI volume	n.s.	n.s.	n.s.	n.s.	n.s.	n.s.
BSO volume & FS volume	n.s.	0.45	n.s.	n.s.	n.s.	n.s.

	Alberta	FESOM	IFREMER	ITU	MITB500	NorESM
Psi & BSO volume	0.71	0.66	0.80	0.54	0.79	0.70
Psi & FS volume	0.48	0.38	n.s.	n.s.	0.48	0.60
BSO volume & BSO heat	0.96	0.94	0.91	0.96	0.94	0.97
BSO heat & SI extent	0.49	0.39	0.37	0.49	0.57	0.61
BSO heat & SI volume	0.44	n.s.	n.s.	0.55	0.48	0.54
BSO volume & FS volume	n.s.	n.s.	n.s.	0.41	n.s.	n.s.

Figure 6. Correlations between key diagnostics from each model. Top, summer (July), and bottom, winter (February). All time series are detrended, and their means are removed. Boxes containing "n.s." mean no significant correlation with a 95% confidence level. Correlations: (1) mean barotropic stream function (Psi) in the Nordic Seas and Barents Sea Opening (BSO) zonal volume transport, (2) mean barotropic stream function (Psi) in the Nordic Seas and Fram Strait (FS) northward volume transport (not net), (3) BSO zonal volume transport and BSO zonal heat transport, (4) BSO zonal heat transport and sea extent in the Barents and Kara Seas, (5) BSO zonal heat transport and sea volume in the Barents and Kara Seas, and (6) BSO zonal volume transport and FS northward volume transport. The JHU model is not included because it uses a repeat-year forcing and does not have realistic interannual variability.

to differ greatly between the models. Second, this connection is not steady in time and appears to vary seasonally. Figure 6 shows correlation values for summer (Figure 6a) and winter (Figure 6b) between different time series for all the model control simulations. Most models have a high correlation between the strength of the barotropic circulation in the Nordic Seas and the volume transport through the BSO (Figure 6). The Alberta model is an exception with no correlation during summer. During winter, however, the correlation is high also for the Alberta model, and higher for all models than during summer, meaning that the relationship between the barotropic circulation in the Nordic Seas and the BSO volume transport is generally stronger during winter. The correlation values between the barotropic circulation in the Nordic Seas and the FS volume transport are generally low, and much lower than for the BSO (Figure 6). During winter, these values are also slightly higher, and the Nordic Seas circulation in NorESM has a relatively high correlation with the FS volume transport ($r = 0.60$). Overall, the relationship between the barotropic stream function and the BSO volume transport is stronger than the relationship between the barotropic stream function and the FS volume transport. Most models show no significant correlation between the northeastward BSO volume transport and the northward FS volume transport. Exceptions are FESOM, which has a correlation of $r = 0.45$ during summer, and ITU, which has a correlation of $r = 0.41$ during winter.

The BSO transport responses to GSM are larger than to GSP (Figures 5 b and 5c), with even greater differences than the Nordic Seas barotropic stream function (Figure 5a). One possible explanation is that in GSM, the Nordic Sea gyre weakens but also contracts, while for GSP it only strengthens but cannot expand. The volume and heat transport anomalies resulting from GSM vary between 0.3 and 1.2 Sv and between 4 and 30 TW, respectively, a reduction of 7–50%. The adjustment time scale of the CRFs in the BSO is also approximately 2 to 3 years, but with substantial response the first year. We believe that the adjustment time scale in the BSO follows directly from the adjustment of the Nordic Seas barotropic circulation. The barotropic response time is days to weeks, but the baroclinic response also has to be taken into account. The baroclinic response time is likely slower due to advection of temperature and salinity anomalies that result from circulation changes.

The wind forcing in the GS is not the only forcing mechanism driving variations in the inflow at the BSO. The inflow is primarily driven by the strength of the local westerly winds following the coastline of northern Norway, which in turn sets up an Ekman transport toward the coast (Furevik, 2001; Ingvaldsen, 2004; Lien et al., 2017; Muilwijk et al., 2018; Sandø et al., 2010). These local wind patterns may or may not correlate with the NAO pattern, and thus the GS wind stress and barotropic stream function in the Nordic Seas. For example, Zhang et al. (1998) and Lien et al. (2017) showed that in recent decades with strong positive NAO index, the BSO AW inflow was strong and had an anomalous eastward extent, but Muilwijk et al. (2018) showed that this relationship is not stationary over long time scales. For the long NorESM control simulation, there is on average a relatively high correlation ($r = 0.5 - 0.8$) between the strength of the barotropic circulation in the Nordic Seas and BSO inflow volume transport, but there are also periods when this relationship completely breaks down, for instance between 1930 and 1950 (Figure S1).

We note that AW exits the Nordic Seas through both the BSO and FS; however, we focus on the BSO and the northeastward flow through the Barents Sea. The dynamics in FS are more complex, with both a northward AW flow in the West Spitsbergen Current, and a southward flow in the East Greenland Current on the western side. Although there is a clear connection between the flow through FS and the circulation in the Nordic Seas (Nøst & Isachsen, 2003), the responses in both inflow and outflow due to the GSP and GSM experiments are less consistent across the models. We believe this is in part because the balance between the BSO AW-branch, the FS AW-branch, and the FS outflow is different across the suite of models we investigated. The FS is also a region with recirculation (Hattermann et al., 2016; Wekerle et al., 2017), and the volume transport varies a lot depending on where the sections are defined (Marnela et al., 2013). Here the models are likely to be different, and the response in recirculation due to GSP and GSM can also differ. Additional complications in the FS are the strong northerly winds, especially during winter, and the steep topography, possibly resulting in large differences in eddy activity depending on model resolution. The complexities of FS demand further investigation using higher-resolution models. However, we discuss the role of the FS branch briefly in section 5.

Although there are some differences among the models, there is a clear relationship between the GS wind stress, the circulation of AW in the Nordic Seas, and the volume transport through the BSO. We find that there is a linear relationship between volume transport anomalies and heat transport anomalies for all models which will be discussed in more detail in the following section.

4.3. Sea Ice Response

The sea ice responses in the NH, and in the combined Barents and Kara Seas, are consistent across the models for the GSP and GSM experiments (Figures 7a and 7b). With an increased GSP wind stress and increased BSO heat transport, all models show a significant reduction of sea ice extent in the Barents and Kara Seas. On average, the annual mean reduction is 50,000 km^2, approximately 5% of the simulated annual mean in the Barents and Kara Sea region. The spatial pattern of sea ice anomalies (Figures 4b and 4c) shows that the response of sea ice area and thickness is confined to the Barents and Kara Seas, North of Svalbard, and the ice edge in the GS, all regions near the AW inflow. Figure 4 shows the NorESM model, but other models behave similarly. As is discussed in the upcoming sections, the response of sea ice in the Barents and Kara Seas occurs mainly during winter. As for the other CRFs, the response of the sea ice cover is also asymmetric between the GSP and GSM cases (Figures 7a and 7b). Due to the reduced GSM wind stress and ocean heat transport through the BSO, all models experience an increase of sea ice extent in the Barents and Kara seas, which is more than double the GSP reduction. The increase in sea ice extent varies from 30,000 to 150,000 km^2, an increase of 3–13%. In general, the sea ice response from the fully coupled Ox-HiGEM model

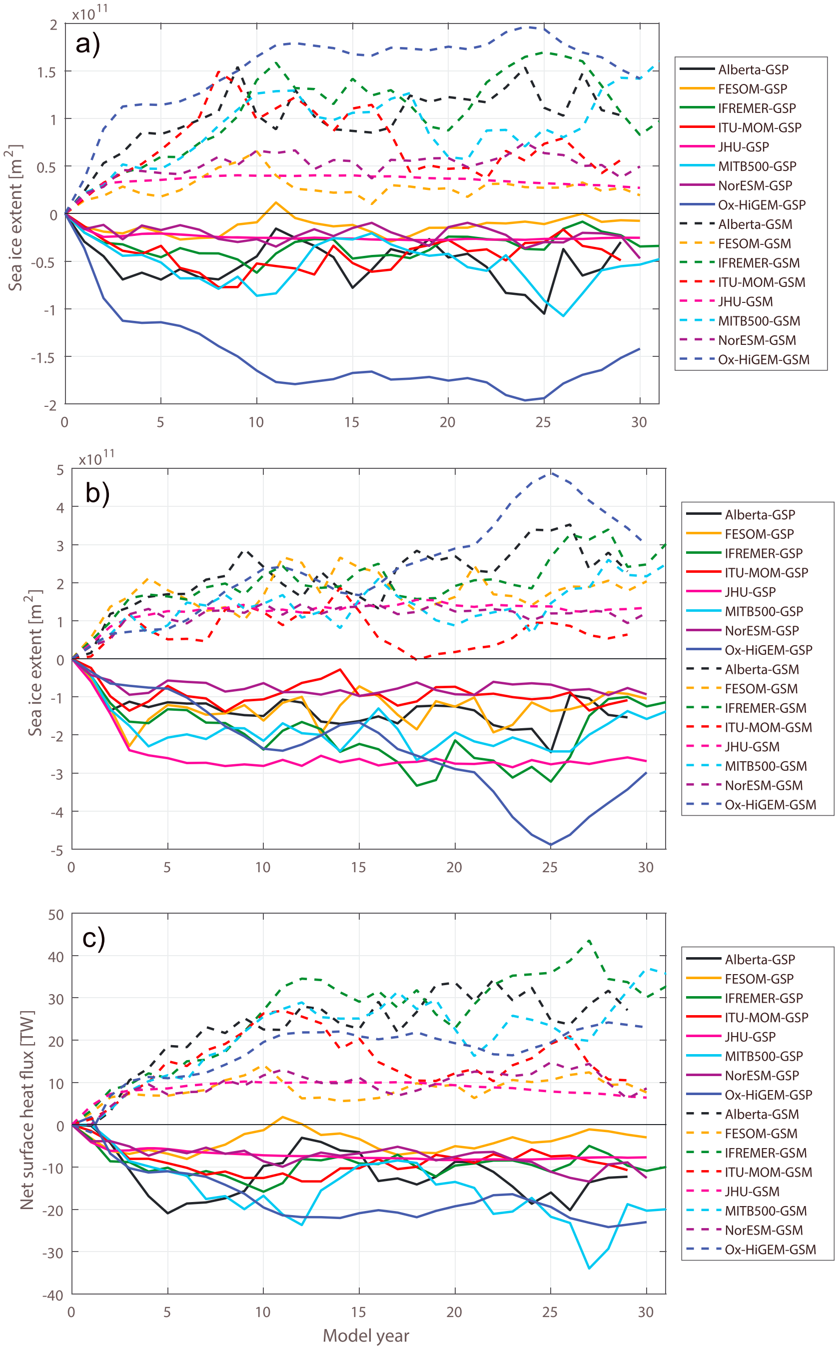

Figure 7. Annual mean climate response functions for sea ice and heat loss. (a) Sea ice extent in the Barents and Kara Seas region, (b) Northern Hemisphere sea ice extent, and (c) spatially integrated net surface heat flux in the Barents and Kara Seas region. The 4-mbar Greenland Sea Plus (GSP) and Greenland Sea Minus (GSM) forcing is shown in Figure 2, and the Barents and Kara Seas area in Figure 1.

is larger than for other models. We believe this is due to the ocean-atmosphere feedback mechanisms related to the surface heat fluxes, which are not captured in the forced simulations. These feedback mechanisms are discussed at the end of the section 4.4. Here it is also important to remember that the Ox-HiGEM responses are symmetric by construction, because we assume linearity. The sea ice extent response in the whole NH is significantly larger than in the Barents and Kara Seas region, mainly due to the large response in the GS (Figure 4). The NH multimodel mean sea ice extent response is approximately 13% for both the GSP and GSM.

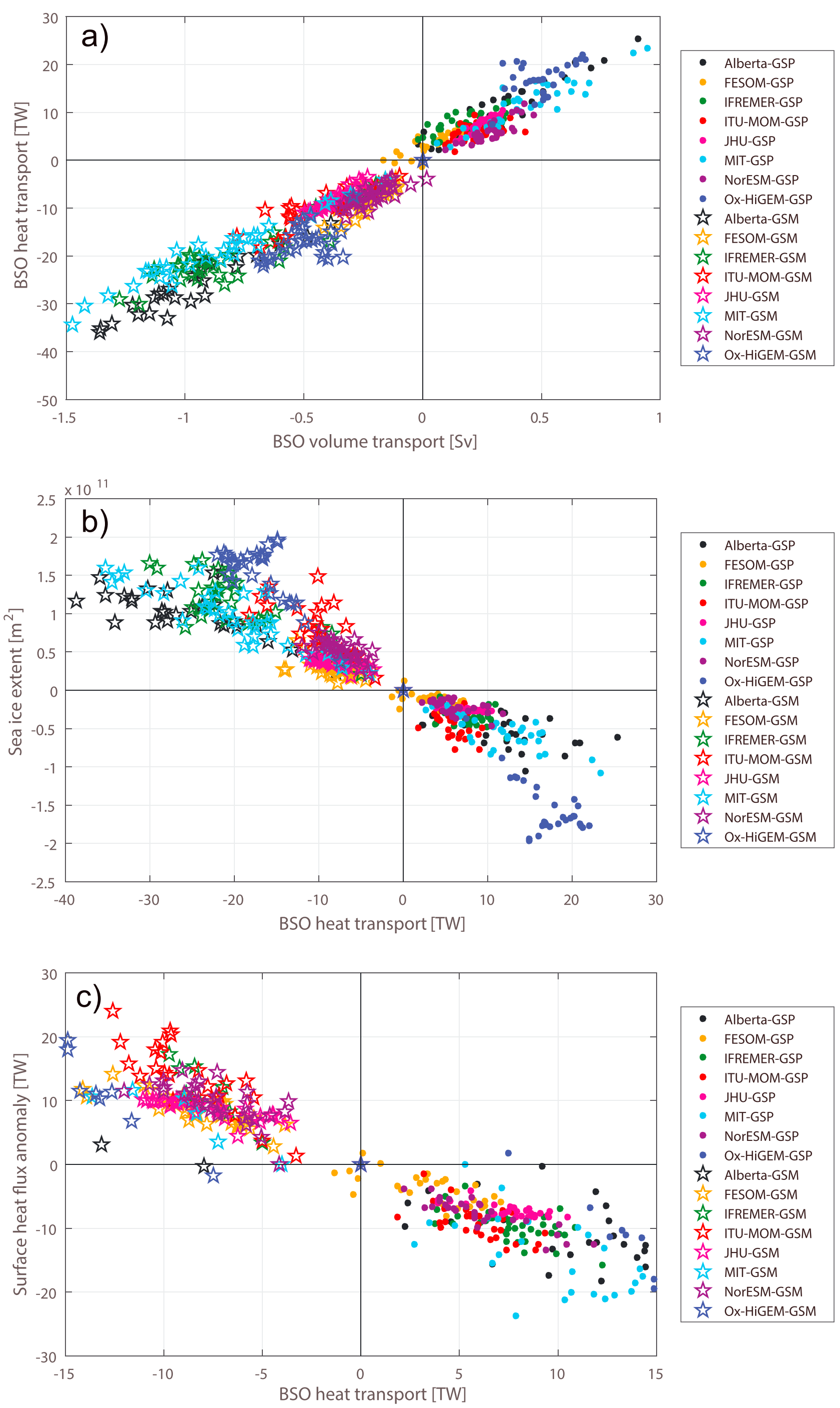

Figure 8. Annual mean values from the climate response functions of Barents and Kara Sea transport, sea ice and heat flux anomalies plotted against each other: (a) heat transport through the Barents Sea Opening (BSO) as a function of volume transport; (b) sea ice extent as a function of BSO heat transport; and (c) integrated net surface heat flux over the Barents and Kara Seas as a function of BSO heat transport. GSP = Greenland Sea Plus; GSM = Greenland Sea Minus.

We find a linear relationship between volume transport anomalies and heat transport anomalies for all models (Figure 8a). There is also a near linear relationship between the advected BSO heat transport anomalies and Barents and Kara sea ice extent anomalies (Figure 8b). Because a larger heat transport leads to less ice, the correlation is negative. On average, a 10-TW heat transport anomaly will result in a change of 50.000 km^2 sea ice area. The direct influence of AW heat anomalies on Barents sea ice has previously been suggested and was estimated by Årthun et al. (2012) to be 70.000 km^2 per 10 TW. An effect of AW heat anomalies has also been suggested for the area north of Svalbard by Onarheim et al. (2014), and here the sea ice is observed to melt effectively if advected over warm AW in the surface layer (Peterson et al., 2017). The AW heat can thus reduce the sea ice cover through direct bottom melt (Sandø et al., 2014) and the reduction of sea ice growth during winter. The latter has been suggested to be the most important in the Barents Sea, and this is why the influence of AW is mainly a winter signal (Onarheim et al., 2018). Another recent study by Barton et al. (2018) showed that since 2005, the winter sea ice edge in the Barents Sea has been restrained by an increase in temperature gradient across the Polar Front, which is a potential vorticity constrained shelf slope current in the eastern Barents Sea. This change may be driven by an increase in AW temperature (Barton et al., 2018). During summer, the Barents Sea is mainly ice free, and therefore, the influence of AW is much smaller.

Changes in sea ice cover involve a complex interplay between atmospheric and ocean forcing. During winter, the ocean often plays a more important role because of the cold air temperatures and lack of solar radiation, but untangling these two driving forces is complicated. In our study, the atmospheric variability in the Barents Sea region is not altered, and only the remote winds are perturbed, which results in an increased ocean heat transport here. We therefore know that the changes in sea ice must largely be related to changes in ocean heat transport. Another possible explanation for altered sea ice cover is changes in sea ice advection. Change in sea ice transport due to GSP and GSM wind anomalies is shown for NorESM in Figure 4d. Response is small in the Barents Sea, but the climatic mean FS sea ice southward export is increased by ~10% due to GSP and decreases similarly for GSM. The downstream GS ice cover increases with GSM for both sea ice thickness (Figure 4c) and extent (Figure 4b) and decreases for GSP, suggesting that the strong GSP winds also bring more AW to the northern GS and melt ice there. It is possible that ice transport anomalies in the Northern Barents Sea explain a part of the sea ice extent anomalies in the Barents and Kara Seas.

Although the response of the sea ice cover is generally consistent across the suite of models, there is some spread in the CRFs, and we believe that this is partly linked to spread in the heat transport CRFs and partly due to differences in the mean sea ice state of the models. For example, models that already have a large sea ice cover experience a small GSM response, and models with a small sea ice cover experience a large increase during GSM. The mean sea ice extent for each of the models is given in the supporting information. NorESM, FESOM, and JHU are the models with smallest GSM response (Figure 7a) and have the largest ice cover in the control simulations. We anticipate a southern maximum limit set by radiative fluxes for the sea ice edge in the Barents and Kara Seas, even with a strongly reduced ocean heat transport. Other models have less ice in their control simulation and therefore grow more ice before they reach the same limit. The forcing of the Alberta model covers a later time period than all other models and therefore has a warmer climatic mean state, and a reduced sea ice cover in comparison to the other models. This might explain why it also has the strongest response during the GSM experiments.

Because the AW influence on sea ice cover in the Barents Sea is mainly a winter signal, we need to ensure that the models have a realistic seasonal cycle. We have therefore compared the variability in the different control simulations to satellite observations. Figure S3 presents a Taylor diagram of the model's seasonal cycle (a) and interannual variability (b), for the time period 1980–2010 in comparison to satellite observations from the National Snow and Ice Data Center (NSIDC; Cavalieri et al., 1996). All models simulate the seasonal cycle well, with correlations higher than $r = 0.97$, but with relatively large differences in standard deviation. There is a relatively large difference between the observed and simulated interannual variability. The ITU-MOM, IFREMER, and FESOM models are closest to the NSIDC variability with correlation coefficients higher than 0.8. The ITU-MOM and FESOM models share the same forcing data set and are therefore expected to have similar variability.

The third from bottom and second from bottom rows of Figure 6 represent the correlation values over the control simulation between the heat transport through the BSO and the sea ice extent and volume in the Barents and Kara Seas. As expected, in summer the correlation values are low. During summer, most of the area is ice free, and the relatively warm atmosphere and incoming solar radiation appear to control the remaining interannual variability. During winter, however, the atmosphere is generally cold; there is no melting due to solar radiation, and hence, we expect the ocean to play a more important role. Indeed, winter correlation values are generally high for all models. There is, for example, a significant correlation (with a significance level of 95%) between BSO heat transport and sea ice extent, with values ranging between $r = 0.37$ and $r = 0.61$. NorESM has the highest correlation ($r = 0.61$), followed by MIT ($r = 0.57$). The

IFREMER model has the lowest correlation ($r = 0.37$) between BSO heat transport and sea ice extent. For most models, with an exception of ITU-MOM, the correlation is higher with sea ice extent than with sea ice volume.

4.4. Air-Ocean Heat Exchange in the Barents Sea

The Barents Sea occupies only 10% of the Arctic Ocean, and the mean depth is 230 m, creating favorable conditions for cooling of the inflowing AW. In wintertime, when the incoming solar radiation is negligible, this heat loss from the ocean increases, but sea ice also limits this ocean heat loss. Figure 9 displays the annual mean net ocean-atmosphere surface heat flux (averaged over the last 10 years of simulation for all models) and the response due to GSP and GSM. Negative values represent a cooling of the ocean. In general, the mean values are negative in the Nordic Seas and the Barents Sea, with the largest fluxes found along the pathway of the North Atlantic Current. As expected, the surface heat fluxes in the Barents and Kara Seas are highly dependent on the sea ice cover. The average values for the integrated surface heat fluxes and sea ice area in the Barents and Kara seas for the control simulations of the different models are given in Table 3. While the JHU and MIT models have relatively low surface heat flux in the Barents Sea, most models are close to the estimated 76 TW for this region (Table 3; Smedsrud et al., 2013). The fully coupled Ox-HiGEM model has three times the net surface heat flux. Models with a small ice cover, such as Alberta and FESOM, generally lose more heat than models with a larger ice cover. For the majority of models the heat loss is largest toward the north, where the atmosphere is colder and cold-air outbreaks occur. A prominent feature in most models is also large heat loss in the West Spitsbergen Current and near the sea ice edge in the GS. In the FESOM, IFREMER, JHU, and NorESM models there is an annual mean surface heating in the Norwegian and Iceland Seas, a feature that is not prominent in the Alberta, ITU-MOM, and MIT models.

Center and right panels in Figure 9 show a consistent response in surface heat fluxes due to GSP and GSM across the suite of models. The stronger atmospheric GSP forcing causes increased northward ocean heat transport, increased heat loss from the Barents Sea, west of Svalbard, and near the sea ice edge in the GS. Due to the faster GSP circulation, less heat is lost in the Norwegian and Iceland Seas, and warmer anomalies reach further north and increase heat loss there. The opposite is true for decreased GSM atmospheric forcing. The response in the Barents Sea is mainly confined to the northern Barents Sea and linked to the retreat of the winter sea ice edge. On an annual basis this region has more open water and therefore loses more heat. The CRFs of the integrated surface heat fluxes over the Barents and Kara Sea are presented in Figure 7c. The multimodel mean response is approximately 10 W/m^2 for GSP and 20 W/m^2 for GSM, approximately 15–30% relative to the control annual mean. The time scale of this response is slightly longer than for the BSO fluxes and sea ice, approximately 10 years. Again, we believe the spread for GSM is mainly connected to the differences in sea ice state. Models with a large mean sea ice cover tend to have a larger response in sea ice during GSP and open up a large area of open water resulting in a large response in surface heat fluxes. The opposite is true for the GSM case. Heat transport anomalies through the BSO may warm the Barents and Kara Seas, enter the deep Arctic basins, or be lost to the atmosphere. A scatter plot of the surface heat flux anomalies versus the ocean heat transport anomalies is shown in Figure 8c. Although the spread between models is slightly bigger than for Figures 7a and 7b, the scatter plot indicates a near linear relationship between the ocean heat transport anomalies and the surface heat flux anomalies. Direct comparison of the surface heat flux anomaly with the ocean heat transport anomaly is difficult since we do not have a closed heat budget. Figure 8c suggests that a large portion of the advected heat anomalies are lost to the atmosphere in the Barents and Kara Sea region. This is mainly because the positive AW heat anomalies prevent formation of sea ice increasing the open-water area, cooling the AW more efficiently. Årthun et al. (2012) showed that the BSO inflow heat transport carries 79% of the annual variance in the net advective heat convergence in the Barents Sea, and 94% if monthly values are considered. The variabilities of the heat convergence and the inflow are thus closely related, and the temperature variability in the water exiting the Barents Sea is small. This supports the theory that most heat anomalies are not advected into the deep Arctic basins but are either completely lost to the atmosphere or change the heat content locally. This is discussed further in section 5.2.

Several positive feedback loops in the coupled Barents Sea ocean-ice-atmosphere system are possible (Smedsrud et al., 2013). For example, increased surface heat loss from the ocean to the atmosphere, resulting from anomalous ocean heat transport, has been proposed to reinforce the ocean heat transport (Ikeda, 1990; Ikeda et al., 2001; Smedsrud et al., 2013). The increased surface heat loss would lead to a reduction in SLP, and hence, the resulting cyclonic atmospheric circulation anomaly would produce stronger westerly winds over the BSO. Smedsrud et al. (2013) also hypothesized another positive “ocean-feedback” mechanism, where the

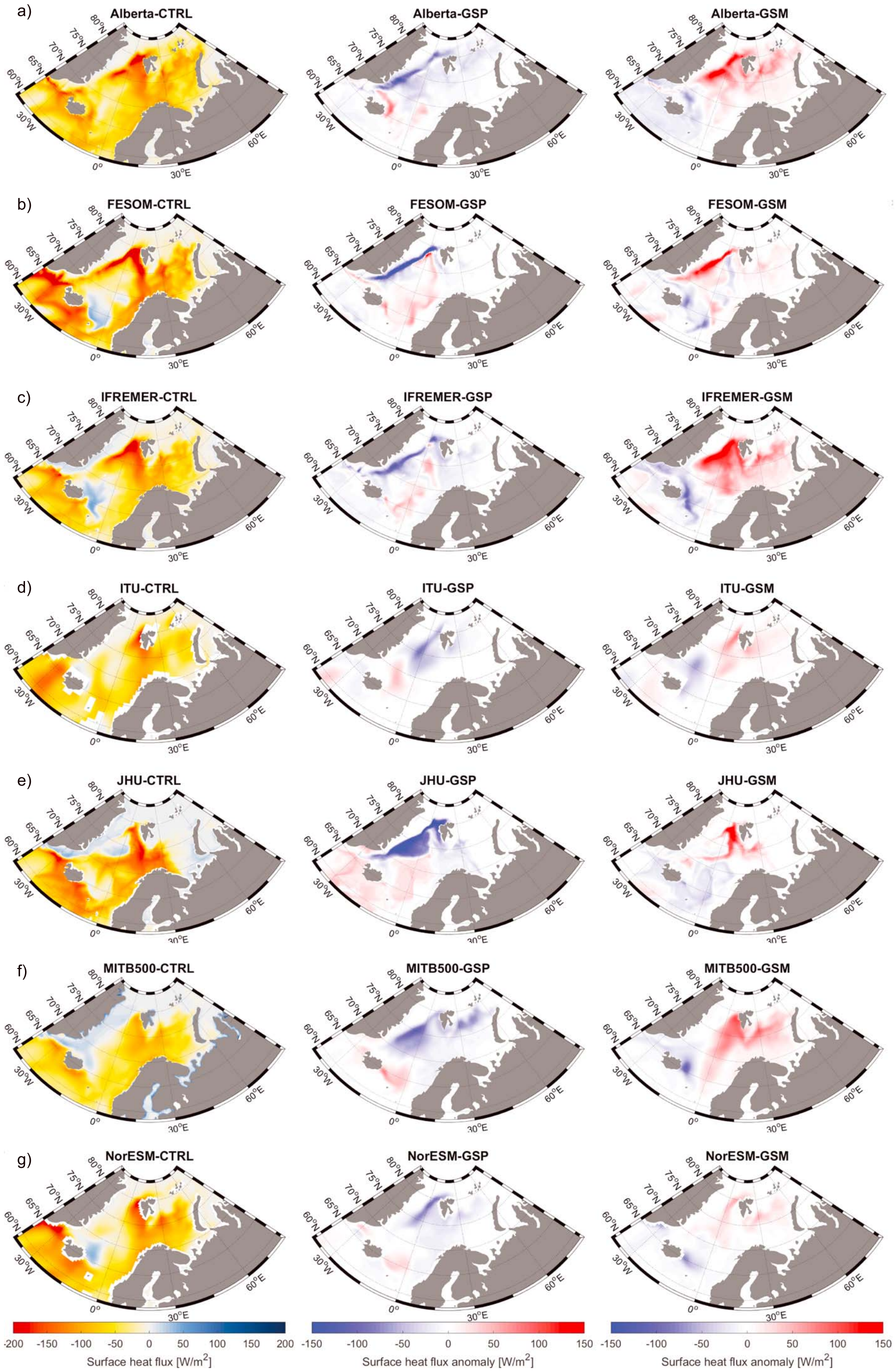

Figure 9. Surface heat flux from the different models. Negative values denote heat loss from the ocean to the atmosphere. Panels on the left show the control simulations, middle panels show Greenland Sea Plus (GSP) anomalies (stronger wind forcing), and right panels show Greenland Sea Minus (GSM) anomalies (weaker wind forcing). All values are averaged over the last 10 years of integration (20–30 years after perturbation).

increased ocean heat loss results in more dense water formation in the Barents Sea and a stronger outflow in the northern Barents Sea, which has to be compensated by a stronger inflow of AW through the BSO.

The models included in Figures 8c and 7c do not include the possibility for any ocean-atmosphere feedback mechanisms, so we believe that the relationship and the response shown there might be different in a fully

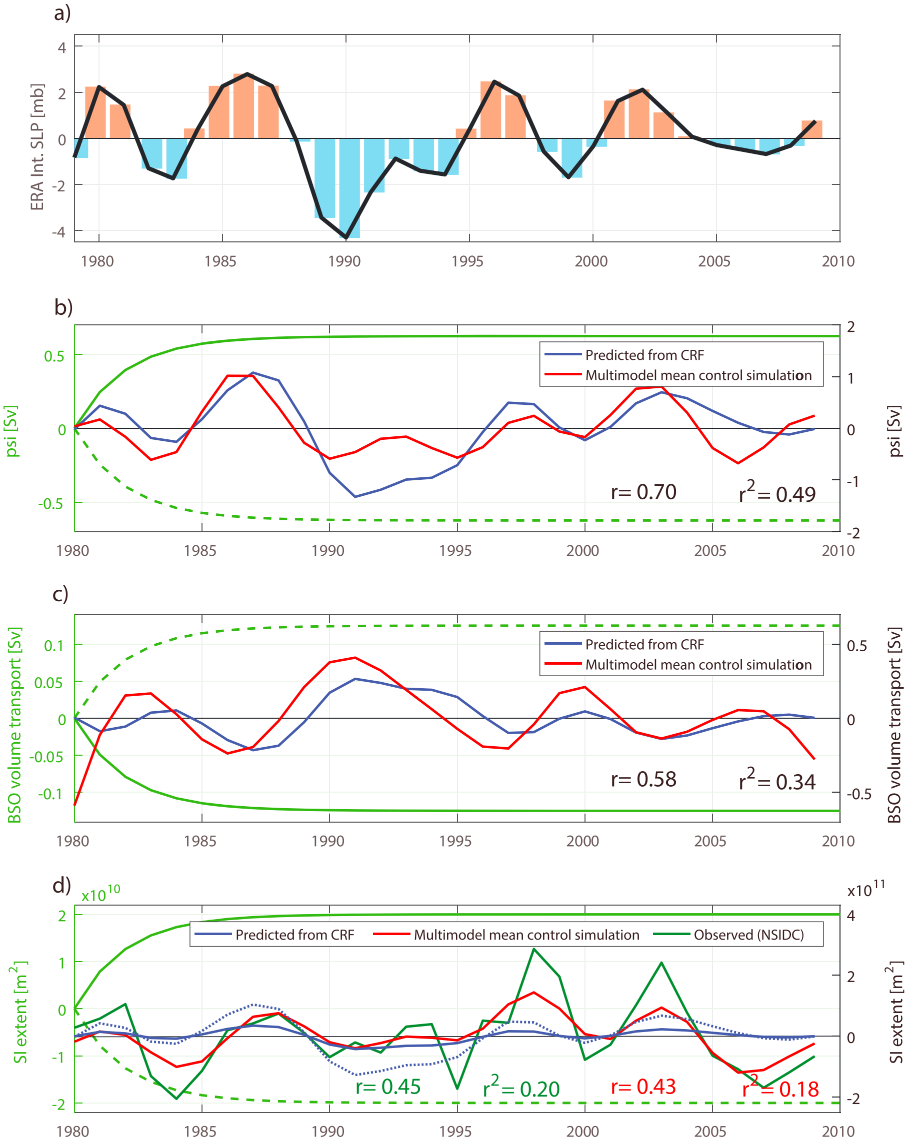

Figure 10. Historical low-pass filtered sea level pressure (SLP) anomalies in the central Greenland Sea from ERA-Interim reanalysis (W_{GS} in equation (4)). (b) Analytical fit (green curves) of the multimodel barotropic stream function climate response function (CRF; C, equation (3)), and anomalous strength of the barotropic stream function, BTS_{NS}, predicted by the CRFs (equation (4); blue curve) and directly simulated by the models (red curve). Note that the green curve has a different scale compared to the red and blue curves and that this is per mb. (c) Analytical fit (green curves) of the multimodel Barents Sea Opening (BSO) volume transport CRF, and anomalous BSO volume transport, VT_{BSO}, predicted by the CRFs (blue curve) and directly simulated by the models (red curve). (d) Analytical fit (green curves) of the multimodel Barents and Kara Seas sea ice extent CRF, and anomalous Barents and Kara Seas sea ice extent, SI_{BK}: observed from National Snow and Ice Data Center (NSIDC; dark green curve), predicted by the CRFs (blue curve) and directly simulated by the models (red curve). Green values denote the correlation between the predicted and the observed time series, and red values denote the correlation values between the predicted and simulated sea ice extent. All time series are detrended. The blue dotted line represents a hypothetical prediction if we assume the CRF has an amplitude three times larger than the multimodel mean.

coupled system. In our simulations, while sea ice cover responds to the changing ocean conditions, the reanalyzed atmospheric forcing remains unaltered and is based on the prescribed sea ice cover of the reanalysis product. Air temperatures over ice covered regions are indeed lower than over open ocean. For new open water regions, these cold temperatures over regions that used to be ice covered will probably be too cold. This is an uncertainty because we only simulate a part of the naturally occurring coupling. For example, the sea ice response to increased AW heat input could be a low-end estimate because of strong heat loss where the atmosphere is too cold. The Ox-HiGEM CRFs are calculated from multiple linear lagged regression in a coupled model control run and, as such, partly incorporate atmospheric feedbacks related to surface heat fluxes. This may explain the stronger Ox-HiGEM sea-ice response.

The negative correlation between BSO ocean heat transport and sea ice extent suggests that ocean variability is an important driver of sea ice variability. The increased ocean heat transport from the GSP anomalies results in a smaller sea ice cover in the Barents and Kara Seas. The larger open water area hence results in increased ocean-to-atmosphere heat fluxes in all models. Similar dependence was found from direct observations by Ivanov et al. (2003) and Smedsrud et al. (2013).

4.5. Convolution of the CRFs and Potential for Prediction

Having described the response resulting from anomalous SLP in the GS and the form of some key CRFs, we now use this to compute the response to a historical time series of SLP anomalies in the GS (Figure 10a). These “hindcasts” are then compared to calculations from the different models and observations. This comparison gives a sanity check on the utility of the CRFs and can provide us with information on how much of the simulated (or observed) variability can be explained by the GS SLP anomalies. The methodology follows the same procedure as described in Marshall et al. (2017). Here, the focus will be on the relationship between the GS SLP anomalies and the CRFs of the barotropic stream function in the Nordic Seas (Figure 5a), BSO volume transport (Figure 5b), and sea ice extent in the Barents and Kara Seas (Figure 7a).

We define C (units Sv/mbar) as the response function per unit forcing of the mean barotropic stream function strength in the Nordic Seas. $\widehat{BTS}_{NS}$ (units Sv) is the amplitude of the resulting change in the barotropic stream function induced by pressure anomalies over the GS. We fit an analytical expression to the multimodel mean CRFs shown in Figure 5a and assume that the responses to GSP and GSM are roughly equal of magnitude but of opposite sign. All calculations have also been performed with the CRFs of the individual models (not shown), but since we did not find notably different results, we have chosen to only present the fit based on the multimodel mean. The following analytical expression broadly captures the form of C:

$$C \times W_{\mathrm{step}} = \widehat{BTS}_{NS}(1 - \exp(-\gamma t)), \tag{3}$$

where the scaling factor W_{step} is the magnitude of the step function in forcing (4 mbar in our case). The time scale of response is very short, as described earlier. An analytical fit based on Figure 5a suggests that $\gamma = \frac{1}{2}\ \mathrm{y}^{-1}$ (i.e., an e-folding response time of 2 years) with $\widehat{BTS}_{NS} = 2.5$ Sv (green lines in Figure 10b). Following equation (1), we may now write

$$BTS_{NS}(t) = \int_0^t C(t - t')\frac{\partial W_{GS}}{\partial t}(t')dt', \tag{4}$$

where W_{GS} (units mbar) is a time series of historical pressure anomalies over the GS, as shown in Figure 10a from the ERA-Interim reanalysis (Dee et al., 2011). We have also tested other reanalysis products, but the results are not sensitive to the product being used. The solution of equation (4) gives us an estimate of the barotropic stream function solely based on GS SLP anomalies and our analytical CRF and is presented in Figure 10b. Unfortunately, there are no observations of the Nordic Seas barotropic circulation strength with which to compare, but comparison with the multimodel mean from the control simulations gives high correlations ($r = 0.7$). These results lend strong support to a close relationship between anomalous SLP in the GS and the barotropic circulation in the Nordic Seas. The success of the convolution in reconstructing the variability in the strength of the Nordic Seas barotropic circulation suggests that almost all of the variability in this circulation is driven by the imposed wind pattern, we have imposed, and that the relationship is relatively linear.

A similar exercise can be repeated for the BSO volume transport, which we will define as VT_{BSO}. As explained above, we can fit an analytical expression similar to equation (3) to the multimodel CRFs shown in Figure 5b. The green curves in Figure 10c represent the fitted analytical response function C (units Sv/mbar) for the BSO volume transport with $\gamma = \frac{1}{2}\ \mathrm{y}^{-1}$ and $\widehat{VT}_{BSO} = 0.5$ Sv. The blue curve in Figure 10c shows the solution of the convolution (as equation (4)) for the BSO volume transport CRF. The estimated volume transport compares well with the simulated multimodel mean, and their correlations are relatively high ($r = 0.58$). The skill on this estimate is somewhat lower than for the barotropic stream function in the Nordic Seas, but this is expected because we are further away from the perturbation location and also expect other mechanisms to influence the variations in the BSO volume transport. For example, the local wind direction in the BSO is likely to be important (Muilwijk et al., 2018). Also, the models we use differ in how well correlated the BSO volume transport is with the Nordic Seas barotropic circulation, and hence with the winds in this region. This will be further discussed in section 5.2. In general, we conclude that there is also a relatively close relationship between anomalous SLP in the GS and the volume transport through the BSO.

Finally, we investigate the convolutions of CRFs from sea ice extent in the Barents and Kara Seas, which we define as SI_{BK}. A multimodel analytical fit of the CRFs presented in Figure 7a is shown in green in Figure 10d. Again, the analytical fit, C (units m^2/mbar), may be expressed like equation (3), now with the coefficients $\gamma = \frac{1}{2}$ y^{-1} and $\widehat{SI}_{BK} = 0.8 \cdot 10^{11}$ m^2. For sea ice extent in the Barents and Kara Seas a good observational record can be obtained from NSIDC passive microwave satellite data (Cavalieri et al., 1996). In Figure 10d, the observed sea ice extent anomalies in the Barents and Kara Seas region are compared with the simulated multimodel mean sea ice extent anomalies, and with the prediction based on the convolution of the analytical CRF and the GS SLP time series (similar to equation (4)). First we would like to point out that although the multimodel mean anomalies are somewhat smaller than the observed anomalies, the correlation between these two time series is high ($r = 0.84$, not shown). The correlation of the time series from individual models with the observed sea ice data was discussed in section 4.3 and can also be seen in the Taylor diagram in Figure S3. Because these are simulations with a forced “realistic” atmosphere, it is expected that they simulate the sea ice variability quite well (Ilicak et al., 2016). The estimated sea ice variability based on the analytical CRF and the GS SLP anomalies is shown in blue in Figure 10d. Its correlation with the observed sea ice anomalies is $r = 0.45$, and the correlation with the simulated multimodel mean anomalies is $r = 0.43$, thus much smaller than for the barotropic flow or the BSO volume transport. Also, the amplitude of the anomalies from the convolution time series is smaller than what is observed and simulated.

The limited success of the reconstructed sea ice variability based on GS SLP anomalies is not unexpected. First, as discussed in section 4.3, there may be several nonlinear responses and feedback mechanisms that are not captured in our CRFs due to the nature of our forced simulations. Hence, we hypothesize that our sea ice response is underestimated (an argument supported by the CRF results from the fully coupled Ox-HiGEM simulation). If our CRFs were to reach an equilibrium that is larger than $\widehat{SI}_{BK} = 0.8 \cdot 10^{11}$ m^2, the estimate would slightly improve. This is illustrated by the dotted blue line in Figure 10d, which shows the convolution based on a hypothetical CRF with an amplitude three times larger than the multimodel mean CRF, and slightly larger than the Ox-HiGEM CRF in Figure 7a. Second, and most importantly, although we do observe a clear linear response in the Barents and Kara Seas sea ice cover following the GS SLP anomalies (Figure 8), there may be other atmospheric and oceanic remote effects that have a potential impact but are not captured in our CRF convolution (Nakanowatari et al., 2014). For example, Onarheim et al. (2015) presented a framework for skillful prediction of sea ice in the Barents Sea based on ocean heat transport, but ocean heat transport is affected by both temperature and volume transport anomalies. Advected temperature anomalies from the south also influence the ocean heat transport into the Barents and Kara Seas (Årthun et al., 2017; Muilwijk et al., 2018). In our CRF experiment we mainly perturb the volume transport.

Hence, we conclude that our CRFs provide a good potential for prediction on relatively short time scales (2 years) of the Nordic Seas barotropic circulation and the BSO volume transport, but not for sea ice extent. The convolutions allow us to produce an estimate of the variability in Nordic Seas circulation directly from knowledge of the winds, without running a model. They also underpin the utility of our perturbation experiments and the value of computing CRFs. Further investigation of the convolution procedure is a current research focus, and this method will likely be refined in future work.

5. Discussion

5.1. Ekman Pumping and the Resulting Circulation

The barotropic circulation results presented in Figure 3 are in accordance with Isachsen et al. (2003), who presented a lowest order theory of the temporal variability for circulation in the Nordic Seas, and related it to Ekman-dynamics. Isachsen et al. (2003) found that anomalous Ekman convergence contributes to a spin-up (or spin-down) of the gyres within regions enclosed by contours of constant f/H, where f is the Coriolis parameter and H is the water depth. In this barotropic model, gyres will spin up cyclonically for cyclonic wind stress anomalies and vice versa. The barotropic response we see from our GSP and GSM experiments is also bounded by f/H contours (not shown) and thus consistent with the simple model of Nøst and Isachsen (2003). However, cyclonic wind stress is likely not the only explanation for the mean cyclonic gyre circulation in the Nordic Seas because baroclinic pressure terms will eventually balance the surface Ekman pumping (Nøst & Isachsen, 2003). The cyclonic circulation in the Nordic Seas and the narrow cyclonic AW boundary current in the Arctic Basin is likely also partially explained by eddy-topography interaction, or the so-called "Neptune effect" (Holloway, 1987).

From Figure 3 we see that there are relatively large differences across the suite of models in regard to the strength and spatial patterns of barotropic circulation. The barotropic circulation is mainly wind driven, and hence dependent on surface stress and Ekman pumping. Nøst and Isachsen (2003) simulated the barotropic circulation in the Arctic Ocean by using the Ekman Pumping and the hydrographic forcing resulting from the geostrophic shear as "forcing terms." The Ekman Pumping velocity (W_{ek}) can be calculated from the surface stress (τ_s) and is given as

$$W_{ek} = \nabla \times \frac{\tau_s}{\rho_0 f}. \tag{5}$$

The hydrographic forcing resulting from geostrophic shear (W_g) can be calculated from the density field and is given as

$$W_g = -V_s \cdot \nabla f / f, \tag{6}$$

where

$$V_s = \frac{1}{\rho_0 f} \mathbf{k} \times \int_{-H}^{0} (\nabla p - \nabla p|_{z=-H}) dz. \tag{7}$$

Here V_s is the geostrophic shear, p the hydrostatic pressure, f the Coriolis parameter, H the water depth, and ρ_0 a reference density of 1,027.8 kg/m^3. Based on their results we explore whether major model differences in the barotropic circulation in the Nordic Seas are a result of either differences in W_{ek} or differences in W_g, the latter being mainly dependent on the mean hydrography. Differences in the resolution dependent representation of bottom topography in the models may also influence the barotropic circulation. The topography might be especially important for the division of the North Atlantic Current into the BSO or FS branches.

Figure 11 shows maps of the annual mean strength of W_{ek} in the control simulations. In general, most models share similar Ekman pumping behavior, but regional differences are visible, particularly in the Barents Sea region. The strongest upwelling is found in the Irminger Basin, Iceland Sea, and southern part of the GS. The strong Ekman pumping in the Irminger Basin is related to the Greenland tip-jet. Nearly all models experience a modest upwelling in the Norwegian Sea and GS, with a minimum in the center of the Basin. NorESM shows relatively large upward Ekman velocities in the GS and Lofoten Basin but also downward Ekman velocities in the central Norwegian Sea. This downwelling is related to the position of the climatological atmospheric low-pressure center in NorESM. While most models experience one large low-pressure system over the Nordic Seas in their long-term mean, NorESM experiences a SLP structure (not shown) with a second low-pressure center centralized over the Lofoten Basin and one low-pressure center over Iceland. Both these centers create Ekman divergences and upwelling, but where they meet in the central Norwegian Sea, they create a convergence zone and downwelling. The wave-like structure in Ekman pumping in NorESM is a result of the topography of Greenland and Iceland. ITU-MOM has the largest regions with strong upwelling in the GS and Irminger Basin.

Relatively strong coastal downwelling is found east of Greenland and Svalbard and is strongest for the FESOM model. All models also experience general downwelling in the Canadian Basin, this is strongest in the JHU model. The values noted in Figure 11 represent long-term average values of the mean Ekman pumping strength for the central Nordic Seas region, and also the mean strength of the Ekman pumping anomalies due to GSP and GSM. From these values we observe that there are relatively large variations in the mean Ekman pumping strength in this region. Spatial maps of W_{ek} anomalies due to the GS experiments are shown in Figure S11.

There is no clear link between the average strength of Ekman Pumping (values noted on Figure 11) and average strength of the barotropic stream function in the same region (Table 3). From the models with relatively low Ekman pumping strength (Alberta, IFREMER, and MIT), only IFREMER and MIT have a relatively weak barotropic circulation. NorESM is another model with relatively weak barotropic circulation, but NorESM has relatively strong Ekman pumping. All models have relatively similar Ekman pumping

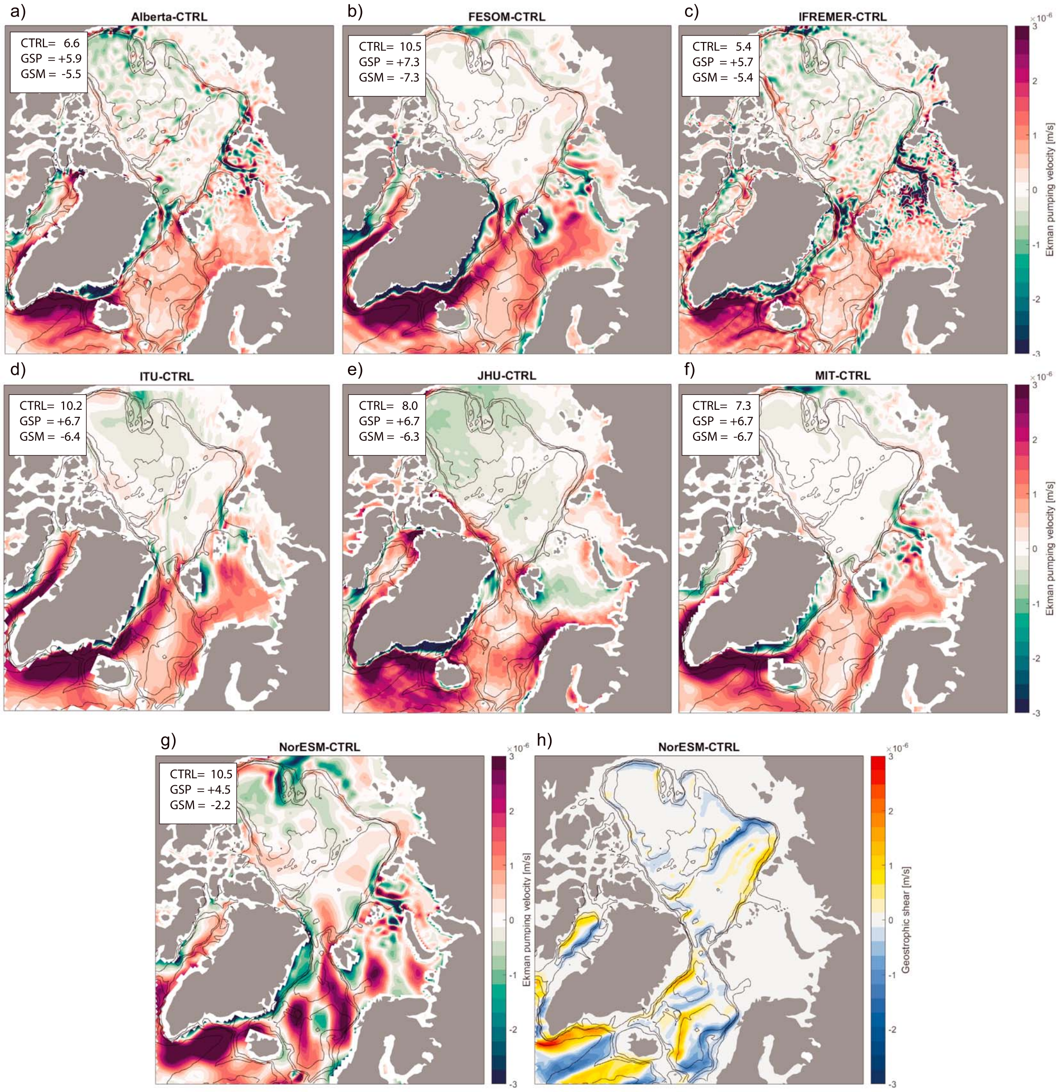

Figure 11. (a–g) Map of the annual mean Ekman pumping ($\nabla \times \tau_s/\rho_0 f$) field computed from the model control simulations. Positive values denote upward velocities. Values in the upper left represent the long-term mean (and anomalies due to Greenland Sea Plus [GSP] and Greenland Sea Minus [GSM]) Ekman pumping averaged over the Nordic Seas region (green box Figure 3). Values are given in 10^{-7} m/s. (h) Map of the annual mean "hydrographic forcing" (given by the geostrophic shear, $-V_s \cdot \nabla f/f$) computed from the NorESM control simulation. All values are averaged over model years 20–25. Black lines show f/H contours. Maps of the spatial anomalies due to GSP and GSM are given in the Supporting Information (Figure S11).

anomalies in response to the GSP and GSM forcings (Figures 11 and S11). NorESM, however, has relatively weak anomalies, and this might explain the relatively weak response for the barotropic stream function (Figure 5a). Based on these results, we hypothesize that differences in the mean (and anomalous) barotropic circulation may partially be explained by spatial differences in the Ekman pumping, possibly related to differences in sea ice cover. Differences in Ekman pumping (Figure 10) may also result from differences in model resolution or differences in the bulk formula, which may impact the barotropic circulation.

Another possible explanation for differences in the barotropic circulation may be differences in mean state hydrography (Nøst & Isachsen, 2003). Differences in hydrography will be manifested in differences in geostrophic currents as a result of equation (7)). The spatial hydrographic forcing from the geostrophic shear (equation (7)) has only been calculated for the NorESM model and is presented in Figure 11h. On average, this forcing results in a much smaller contribution compared to the Ekman pumping contribution. However, where f/H contours are close to each other, the geostrophic shear is relatively large. The GS is such a region with relatively large topographic changes. Differences in mean state hydrography here will likely result in different geostrophic shear in this region, which will in turn affect the barotropic circulation. As is shown in section 5.2, the models have substantial differences in hydrography in this region, making this a plausible partial explanation for the differences in barotropic circulation. The GS is also a region with convective mixing resulting in colder and fresher waters at intermediate depth. Differences in convective mixing in the models may thus also affect the mean state hydrography here, and hence the circulation.

5.2. Fate of the AW Heat Distribution and Its Dependence on the Wind

Local increase and decrease in wind stress affects the barotropic circulation strength in the Nordic Seas and the northward heat transport through the Barents Sea (Figure 5). But how far into the Arctic Ocean basins does this anomaly propagate? The GS wind likely also affects the division of the North Atlantic Current between the BSO and FS and, as is described in further detail in section 5.3, it also affects the AW pathways inside the Arctic Basin. The fate of the ocean heat carried by the FS and BSO branches is substantially different. The BSO branch releases a vast amount of heat to the atmosphere in the Barents Sea (Figure 7c), resulting in a strong local cooling of the AW and relatively cold outflow through the St. Anna Trough into the Arctic Basin. Where the FS branch meets the sea ice edge north of Svalbard, the upper layer melts ice, but at intermediate depth the AW continues into the Arctic Basin releasing heat more gradually over a much larger area (Rudels et al., 1996). Changes in the division of the North Atlantic Current between the FS and BSO will likely affect the fate of the AW heat.

Total vertically and horizontally integrated heat content relative to a reference temperature of 0 ° C shows a clear evolution over time for the different regions (Figure 12, left panels). For the Nordic Seas (Figure 12a), there is an overall cooling for stronger GSP wind stress and warming due to weaker GSM wind stress across the suite of models. This is mainly the result of a temperature change of the upper 1,000 m, which can be observed from the long-term mean profiles (Figure 12b). On average, the models experience a warming or cooling of 0.1–0.5 ° C in the Nordic Seas AW layer as a result of the wind perturbations. Generally, cooling is associated with a slight freshening of the AW layer and warming is associated with a slightly saltier AW layer. Change in the vertically integrated heat content comes from changes in the surface heat fluxes (increased or decreased heat loss) and heat flux divergence due to lateral fluxes. The anomalies in heat content are, consistently in all our models, largely explained by changes in lateral fluxes, but local processes in the Nordic Seas are also important, and these result might be slightly different in a system with a coupled atmosphere. We note that there are also substantial differences in the mean Nordic Seas hydrography for the different models. NorESM and IFREMER generally have a cold and shallow intermediate layer, while the ITU-MOM model, for example, has a very deep and warm intermediate layer. These differences translate into large differences in total heat content for the control simulations.

Concerning changes in lateral fluxes, we hypothesize that the reduction in heat content in the Nordic Seas in the GSP case is mainly a result of enhanced AW export in the north and enhanced import of cold Polar Water in the EGC. Another process causing decreased heat content under the GSP forcing is increased Ekman pumping leading to a lifting of the colder water (around 0° C) from below 1000 m. The gyre spin up is associated with a doming of deep isopycnals, and import of more cold deep water from outside the domain, which then contributes to a general decrease of heat content. Tesdal et al. (2018) showed that this also happens in the Subpolar Gyre. Concerning local forcing, the stronger winds lead to stronger heat loss by increasing the turbulent fluxes of sensible and latent heat. Asbjørnsen et al. (2019) have recently shown that 50% of the variability in the Nordic Seas ocean heat content can be attributed to local surface forcing, and although we have not investigated this in depth, we speculate that the changes in heat content arise due to a combination of advection and local forcing. Note that the accelerated Norwegian Current (and resulting greater heat transport from the south) is mainly excluded from the Nordic Seas box shown in Figure 3.

The CRFs of heat content in the Barents and Kara Seas region are shown in Figure 12c. Although the responses are less consistent between models than in the Nordic Seas, most models, with the exception of MIT and JHU, experience an increase in total heat content due to GSP and decrease due to GSM. An increase in heat content is consistent with the increase in heat transport through the BSO (Figure 5) and associated with a slight warming of the whole water column (Figure 12d). The opposite is true for the decrease. This is consistent with Årthun et al. (2012) and strengthens the theory that heat anomalies advected through the BSO mainly affect the surface heat fluxes (Figure 8c) and the heat content locally. A closed heat budget anal-

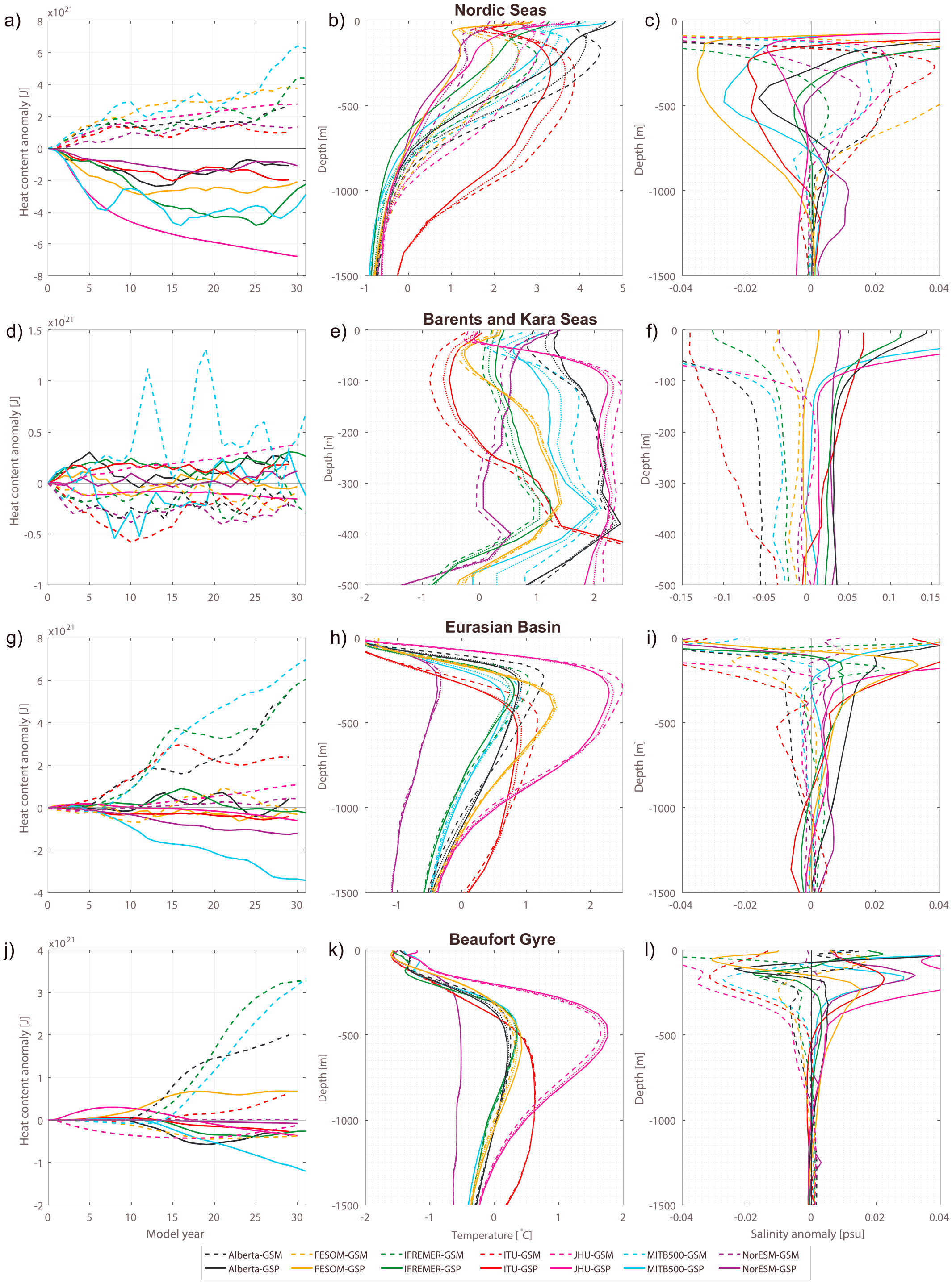

Figure 12. Arctic Ocean heat anomalies, mean temperature profiles, and salt anomalies. Left: climate response functions of vertically and horizontally integrated heat content relative to 0 ° C for the Greenland Sea Plus (GSP) and Greenland Sea Minus (GSM) wind anomalies. Solid lines represent the GSP simulations, and dashed lines represent the GSM simulations. Note that GSP implies a stronger cyclonic forcing over the Nordic Seas and increased barotropic circulation strength in the Nordic Seas. Heat content is calculated over the full depth. Middle and right: annual mean temperature profiles and salinity anomalies for the different basins and models averaged over the last 10 years of integration (20–30 years after perturbation). Solid lines represent the control simulations, dotted lines represent the GSP simulations, and dashed lines represent the GSM simulations. Note that for temperature the actual profiles are shown, but for salinity, only the anomalies are shown.

ysis is needed to confirm this. The only models that do not experience a warming in the Barents and Kara Seas region are MIT and JHU. This might be due to changes in sea ice cover, such that heat loss outweighs the increased heat input. The temperature distribution in the Barents and Kara Sea is relatively uniform throughout the water column, but there are large contrasts between the models, with a difference of more than 2 ° C. We believe this is mainly due to advection.

The GSP and GSM perturbations have a consistent impact on the heat content in the deep Arctic Basins (Figure 12). The response here is delayed, but after approximately 5 years all models experience an increase in heat content in the Eurasian Basin as a result of the GSM perturbation. The MIT, JHU, NorESM, and ITU-MOM models also experience a decrease in heat content in the Eurasian Basin resulting from GSP, but Alberta, IFREMER, and FESOM show no clear response.

There is also a response downstream in the Beaufort Gyre. As in the Eurasian Basin, most models experience a small decrease in heat content from GSP and a slightly larger increase in heat content due to GSM. During GSP the AW layer in the Beaufort Gyre becomes slightly colder and saltier, and during GSM, the AW layer becomes warmer and fresher. It seems likely that less ice and larger surface heat loss in the Barents Sea during GSP result in colder water ultimately entering the Eurasian Basin. After approximately 10 years this anomaly is subsequently advected into the Beaufort Gyre. The opposite is true for GSM, with the AW entering the Arctic through the St. Anna Trough retaining more of its heat due to a more extensive ice cover and less heat loss in the Barents Sea. As is shown from passive tracer results (section 5.3), during GSP, more AW enters the deep Arctic Basins. Because more AW volume is inconsistent with a decrease in heat content, the temperature of the AW must be lower. It is to be noted that the GSP and GSM anomalies are relatively small, and smaller than both the anomalies from the individual models and the differences between the different models. Overall, the effect of the GSP and GSM experiments on the Beaufort Gyre region is not very strong. The FESOM and JHU models show the opposite responses to the other models in the Beaufort Gyre. In section 5.3 we show that the FESOM model is the model with least response in total AW volume in the deep Arctic Basins, which might explain the lack of response in heat content. The JHU model may behave similarly, but unfortunately, this model did not have passive tracers implemented.

Generally, the models have a more similar hydrography in the Eurasian Basin and Beaufort Gyre, but NorESM stands out with a cold bias, and ITU-MOM with a slight warm bias. This is well known and discussed in detail in Ilicak et al. (2016). JHU has a warm bias only in the AW layer. We hypothesize that the change in heat content in the deep Arctic basins is mainly connected to the increased or decreased cooling of AW in the Barents and Kara Seas, and the changing circulation pathways. The lack of response in the Eurasian Basin in the Alberta and IFREMER models might result from redistribution between the different basins. Possibly, the AW is colder, but at the same time more AW stays in the Eurasian Basin. These two processes might outweigh each other. Unfortunately, the IFREMER and Alberta models did not have passive tracers implemented to allow us to check this.

5.3. AW Flow From Passive Tracer Release

To further investigate the circulation of AW, we consider the advection and diffusion of passive tracers that were released in four of the models. These tracers were released continuously at three locations along the AW flow path for approximately 30 years, starting in 1980 (Svinøy, BSO, and FS). Figure 13 shows the mean concentration of a passive tracer 20–25 years after release in the BSO. The tracer concentrations are standardized by depth in order to visualize the differences between the shallow Barents Sea and deep Eurasian Basin. By this we mean that all tracer volumes have been divided by water depth, and it can be interpreted as a fraction of the water column that is filled with tracer. Figures S6 and S7 show the same for the Svinøy and FS tracers. For the BSO tracer we also show the surface concentration and the concentration at the depth of the AW layer (400 m) in Figures S12 and S13, respectively. Most of the Barents Sea is quickly filled up with AW from the BSO, and this eventually enters the Eurasian Basin through the St. Anna Trough. In all models the AW continues to circulate cyclonically in the deep Arctic basins, but the bulk does not cross the Lomonosov Ridge and remains in the Eurasian Basin. After some modification, here the AW circulates back to the Nordic Seas through FS. Animations of these passive tracer concentrations are available in the supporting information.

The tracer release experiments reveal substantial differences in advection between these four different control simulations (Figure 13). The ITU-MOM and FESOM models have the strongest circulation inside the Arctic Basin, where a substantial portion of the BSO tracer ends up in the Canadian and Makarov basins. In

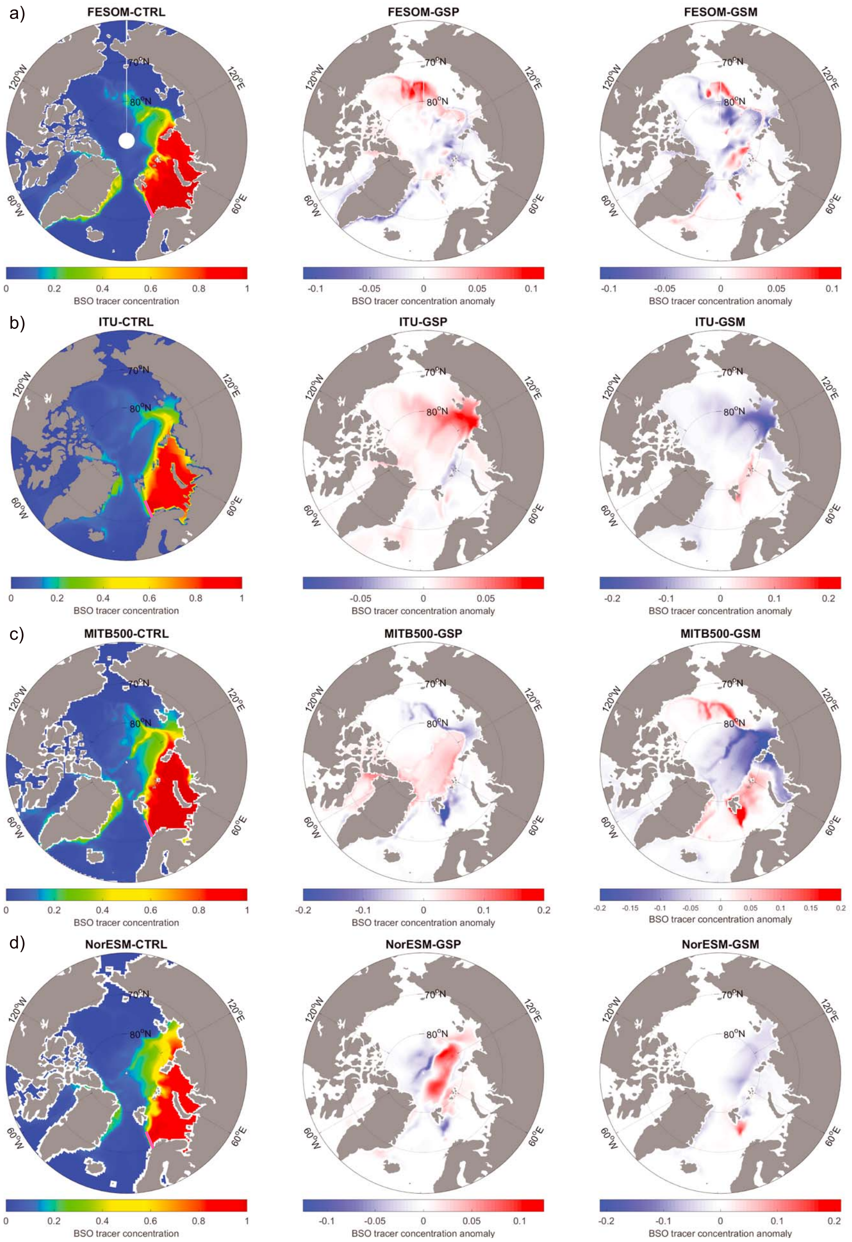

Figure 13. Vertically integrated concentration of passive tracer released continuously at all depths in the Barents Sea Opening (BSO) in four models. Panels on the left show the control simulations, middle panels show anomalies resulting from the GSP experiment (stronger wind forcing), and right panels show anomalies resulting from the GSM experiment (weaker wind forcing). All values are averaged over model years 20–25. Tracer release started simultaneously with the beginning of the perturbation. All values are standardized by depth. The pink line marks the tracer release location.

the MIT simulation less of the BSO tracer crosses the Lomonosov Ridge, and most of the BSO tracer remains in the Eurasian Basin, whereas in NorESM nearly none of the BSO tracer crosses the Lomonosov Ridge. Observations of the circulation in this area are scarce, but Karcher et al. (2012) make the point that the ability of the AW to cross the Lomonosov Ridge might vary over time. One possible explanation is that the MIT and the NorESM models create more dense water in the Barents Sea, and this subsequently has trouble crossing over the Lomonosov Ridge. This is likely related to numerics in the model. The Lomonosov Ridge creates a potential vorticity barrier, so differences between the momentum advection schemes and momentum closure schemes (i.e., viscosity operator) might lead to differences among the models. The tracers released in the FS and at Svinøy also show that there are large differences in how much of the AW recirculates in the

FS. Both MIT and NorESM have relatively high recirculation in the FS whereas ITU-MOM and FESOM generally transport AW further into the Arctic Ocean (Figures S6 and S7).

In general, GSP results in an increased volume of BSO tracer in the deep Arctic Basins for all models and vice versa for GSM after 20–25 years (Figure 13). Because the heat content of these basins goes down (Figure 12), this AW must be colder than before. There is a very limited response in the Barents and Kara seas, because these regions were already filled with AW from the BSO. However, the spatial distribution is also very different from the control simulations. For NorESM and MIT, the AW originating from the BSO and the FS (Figures S6 and S7) is more confined to the southern part of the Eurasian Basin in the GSP case. Here, the Nansen Basin experiences an increased volume of AW, while the Amundsen Basin experiences a decreased volume of AW after 25 years. More AW enters the Arctic Basin in the GSP case, but it does not reach as far north and west into the deep basins. For these two models the increased circulation results also in a quicker recirculation and shorter residence time; as more AW enters, the "throughflow" in the Arctic Basin increases, and more AW exits through FS. This could also contribute to a lower heat content. The opposite is true for the GSM case, where a lower wind stress in the Nordic Seas results in less AW in the deep Arctic Basins. For MIT there is a positive AW volume anomaly in the Makarov and Canadian basins for the GSM case, meaning the AW reaches further to the north and west when the circulation is weak. This contributes to the positive anomaly in heat content of the Beafort Gyre in the GSM case (Figure 12).

The ITU-MOM and FESOM models behave slightly differently than MIT and NorESM. The ITU-MOM model also experiences an increased AW volume in the deep Arctic basins in the GSP case, but here the increase mainly results in more tracer volume further away from the inflow region, toward the Laptev Sea, Makarov Basin, and Canadian Basin (Figure 13). This increase is Arctic-wide for ITU-MOM, but with the strongest response in the Laptev Sea. Because this increase of AW volume is related to a decrease in heat content (Figure 12), the AW must be colder than before. FESOM actually experiences a decrease of AW volume in the Nansen Basin and an increase in the Makarov and Canadian Basins. For FESOM, the GSP case does result in a longer AW residence time in the Arctic Basin, and hence less AW volume in the outflowing East Greenland Current. In the GSM case, the ITU-MOM model also experiences an overall decrease of AW volume in all the deep Arctic basins. Again, the response is strongest in the Laptev Sea. For FESOM there is also a general decrease in AW for GSM, but also a small increase in the Nansen Basin and the southern parts of the Canadian Basin. In the Barents and Kara Seas we see an initial response due to the stronger circulation, which tells us that the Barents and Kara Seas fill up with AW faster due to the GSP perturbations and slower due to the GSM perturbations. In 20 years an equilibrium is reached because the seas are completely filled with AW originating in the BSO. The BSO tracer increases steadily in the Eurasian Basin during the GSP case for the ITU-MOM, MIT, and NorESM models and vice versa for GSM. The FESOM model has an initial response, which is similar to the other models, but in the long term there is no change in absolute tracer volume in the Eurasian Basin. Overall, in the Eurasian and Canadian Basins, an increase of total AW volume is related to a decrease in total heat content, thus the AW temperature is lower than before. The model with least clear response in AW volume in these deep basins (FESOM) is also the model with the smallest response in heat content change.

The change in temperature in the Eurasian Basin has been investigated thoroughly for the NorESM (Figure S5). The average annual mean temperature shows a thick near-surface layer of relatively warm AW entering through FS. This layer cools but continues at depth toward the Laptev Sea. We note that NorESM has a cold bias (Ilicak et al., 2016) and that the absolute temperatures are therefore too low. The GSP perturbation results in a stronger AW circulation and a warmer intermediate and surface layer, but colder temperatures at depth and near the inflow region (Figure S5b). This is consistent with a stronger throughflow in the Nordic Seas combined with a more effective lifting of the colder deep water due to the stronger GSP wind forcing. In the Eurasian Basin the temperatures are colder from the surface to the bottom, apart from just downstream of the FS at intermediate depth. As discussed in section 5.2 this is likely due to the stronger "throughflow" and cooling in the Barents Sea, increasing the proportion of AW that has been effectively cooled and densified, and which ends up at depth in the Eurasian Basin. The cooling could also result from increased transport of colder waters from the Western Arctic.

We conclude that the changing GS wind forcing clearly affects the AW pathways and its residence time in the different seas and basins of the Arctic Ocean. Likely, the strength of the barotropic circulation also affects the vertical distribution, temperature, and possibly also salinity of the AW in the Arctic Ocean. When it comes to the AW pathways, there are, however, larger differences across the suite of models, both in the mean state and in the responses.

6. Summary and Conclusions

We have here analyzed a suite of different Arctic Ocean model simulations to understand the effect of anomalous wind forcing over the GS. We examined similarities and differences in Nordic Seas circulation, poleward ocean heat transport, AW pathways, and Arctic sea ice. This coordinated model comparison grew out of the Forum for Arctic Modeling and Observational Synthesis community, and one main goal here is to compute CRFs for the Atlantic sector of the Arctic Ocean to understand climate and model sensitivity to changes in wind forcing. We have successfully shown that CRFs based on SLP anomalies have a potential for prediction purposes and that there is a clear link between the GS winds, northward ocean heat transport, and sea ice. Overall, there is a strong general agreement between the different models, but for some aspects the models behave differently and had different biases, which underlines the value of doing cross-model comparisons.

We focus on the sensitivity of AW circulation to stronger and weaker GS winds. The stronger wind forcing, termed GSP, is the geostrophic wind increase related to a 4-mbar drop in surface pressure in the central GS. The weaker forcing is opposite in strength and termed GSM, and they are both comparable to observed Nordic Seas annual mean SLP anomalies that resemble the NAO variability.

A stronger GS wind stress results in stronger cyclonic barotropic circulation in the Nordic Seas and increased northward transport of AW volume and heat through the BSO. A weaker GS wind stress results in the opposite. The responses in the BSO have a response time of 1–5 years where most of the response happens during the first year after the perturbation begins. The change in AW flow extends from south of the Subpolar Gyre, through the Nordic Seas, and all the way north into the Canadian Basin. There is a corresponding net decrease in the depth-integrated heat content in the Nordic Seas, Eurasian Basin, and eventually in the Canadian Basin due to GSP. This net decrease in Nordic Seas heat content is likely connected to increased input of cold water from the north, uplifting of cold waters from the deep ocean, and increased heat loss within the Barents and Kara Seas. In a similar way, the weaker GSM forcing leads to an increased depth-integrated heat content along the AW inflow pathway.

The GS experiments impact the AW flow all the way downstream into the Canadian Basin, but overall, the effect of the GSP and GSM experiments on the Beaufort Gyre region is not very strong. During GSP, the AW layer in the Beaufort Gyre becomes slightly colder and saltier, and during GSM, the AW layer becomes warmer and fresher. The response in this region is relatively small, and the GSP/GSM anomalies are not larger than the temporal anomalies in the control simulations from the individual models or the differences between the different models.

The higher GS wind stress of the GSP experiment results in an increased transport of warmer AW into the Barents and Kara Seas. Likewise, the weaker GSM wind stress leads to a smaller AW inflow volume transport. This response is clear in all models, but the strength of the response varies. The most remarkable result is the very close-to-linear response in the heat transport into the Barents Sea, the heat content in the Barents/Kara Seas, the heat loss to the atmosphere, and the change in sea ice extent. The response integrated over the whole Arctic amounts to a loss of about 10% of the annual mean sea ice area for a 4-mbar SLP anomaly over the GS. The positive AW inflow volume anomaly due to GSP leads to a higher ocean heat transport into the Barents Sea, a local warming, less sea ice, and a stronger heat loss to the atmosphere. The opposite is true for the weaker GSM forcing. This response is similar to the main cause of Barents Sea variability examined over the last 2,500 years by Smedsrud et al. (2013), but our results increase the confidence in this response by demonstrating that it appears across a suite of models.

The CRFs have a 2- to 5-year dynamic adjustment time, suggesting that there is potential for predictability on these time scales. A reconstruction of the strength of the barotropic circulation in the Nordic Seas based solely on a linear convolution of SLP anomalies in the GS with the CRFs explains 49% of the variance simulated by the models. Also, for the AW volume transport into the Barents Sea there is high correlation ($r = 0.58$) between the CRF hindcast and the direct calculations from the models, explaining approximately 34% of the variance. For sea ice extent, the reconstructions based on GS SLP anomalies are not well correlated with observed or simulated variability. This is likely due to a combination of missing ocean-atmosphere feedback mechanisms and the fact that there are other major forcing mechanisms influencing ocean heat transport and sea ice extent. One of these important mechanisms, which are captured to limited extend in our CRF prediction, is the propagation of temperature anomalies from the south, which Årthun et al. (2017) has shown also strongly affect the ocean heat transport and, hence, the sea ice extent in the Barents Sea.

Increased ocean heat transport into the Barents Sea results in an increased net surface heat loss, and a net cooling effect on the AW that exits the Barents Sea. As most of our models are forced with atmospheric reanalysis, this strong cooling might be overestimated because the atmosphere is not able to respond to such increased heat fluxes. This is not the case for the CRFs from the Ox-HiGEM group, which are calculated by multiple linear lagged regression in a fully coupled ocean-ice-atmosphere simulation. Consequently, the response in sea ice is stronger in this coupled system, because there is less heat loss to the atmosphere to dampen the initial sea ice loss, and more AW heat available to prevent sea ice growth. The Ox-HiGEM results show that ocean-atmosphere feedback mechanisms in the Barents Sea are important and that the sea ice response might be underestimated in the forced simulations we focus on here.

Passive tracers show that anomalous wind stress in the Nordic Seas results in different AW pathways in the Arctic Ocean. This is consistent with Ilicak et al. (2016), who found substantial differences between Arctic Ocean simulations. Differences in barotropic circulation between models can be attributed to different climatological states, differences in AW pathways, and differences in Ekman pumping. The details of the circulation pathways, including the relative intensity of AW recirculation, FS, and Barents Sea inflows, will likely depend on the exact position of the wind anomaly, but we nevertheless expect the conclusions drawn here to be robust. In general, the CRF approach appears valuable for comparing climate models and their response to key drivers of climate variability, and for extracting the governing processes within the large and dynamic present-day changes occurring in the Arctic Ocean.

Author Contributions

John Marshall had the initial idea to compare Arctic Models using Climate Response Functions, and the different model simulations were run by the different groups. Data analysis was done by Morven Muilwijk in collaboration with Mehmet Illicak. Morven Muilwijk wrote the text with input from Lars H. Smedsrud, and all authors contributed to describing their own model and suggested improvements.

References

ACIA-Arctic Climate Impact Assessment (2005). *Arctic climate impact assessment*. Cambridge: Cambridge University Press.

Aagaard, K. (1970). Wind-driven transports in the Greenland and Norwegian seas. *Deep Sea Research and Oceanographic Abstracts*, *17*, 281–291. https://doi.org/10.1016/0011-7471(70)90021-5

Aagaard, K., Foldvik, A., & Hillman, R. S. (1987). The West Spitsbergen Current: Disposition and water mass transformation. *Journal of Geophysical Research*, *92*(C4), 3778–3784. https://doi.org/10.1029/JC092iC04p03778

Aagaard, K., Swift, J. H., Jolla, L., Carmack, E. C., Vancouver, W., & Columbia, B. (1985). Thermohaline circulation in the Arctic. *Deep Sea Research Part I: Oceanographic Research Papers*, *90*, 4833–4846. https://doi.org/10.1029/JC090iC03p04833

Årthun, M., & Eldevik, T. (2016). On anomalous ocean heat transport toward the Arctic and associated climate predictability. *Journal of Climate*, *29*(2), 689–704. https://doi.org/10.1175/1301JCLI-D-15-0448.1

Årthun, M., Eldevik, T., Smedsrud, L. H., Skagseth, O., & Ingvaldsen, R. B. (2012). Quantifying the influence of Atlantic heat on Barents sea ice variability and retreat. *Journal of Climate*, *25*(13), 4736–4743. https://doi.org/10.1175/JCLI-D-11-00466.1

Årthun, M., Eldevik, T., Viste, E., Drange, H., Furevik, T., Johnson, H. L., & Keenlyside, N. S. (2017). Skillful prediction of northern climate provided by the ocean. *Nature Communications*, *8*(May), 15875. https://doi.org/10.1038/ncomms15875

Årthun, M., & Schrum, C. (2010). Ocean surface heat flux variability in the Barents Sea. *Journal of Marine Systems*, *83*(1-2), 88–98. https://doi.org/10.1016/j.jmarsys.2010.07.003

Asbjørnsen, H., Arthun, M., Skagseth, Ø., & Eldevik, T. (2019). Mechanisms of ocean heat anomalies in the Norwegian Sea. *Journal of Geophysical Research: Oceans*, *124*, 2908–2923. https://doi.org/10.1029/2018JC014649

Bamber, J., van den Broeke, M., Ettema, J., Lenaerts, J., & Rignot, E. (2012). Recent large increases in freshwater fluxes from Greenland into the North Atlantic. *Geophysical Research Letters*, *39*, L19501. https://doi.org/10.1029/2012GL052552

Barnier, B., Madec, G., Penduff, T., Molines, J.-M., Treguier, A.-M., Le Sommer, J., et al. (2009). Impact of partial steps and momentum advection schemes in a global ocean circulation model at eddy-permitting resolution. *Ocean Dynamics*, *59*(3), 537. https://doi.org/10.1007/s10236-009-0180-y

Barton, B. I., Lenn, Y.-D., & Lique, C. (2018). Observed Atlantification of the Barents Sea causes the polar front to limit the expansion of winter sea ice. *Journal of Physical Oceanography*, *48*(8), 1849–1866. https://doi.org/10.1175/JPO-D-18-0003.1

Bentsen, M., Bethke, I., Debernard, J. B., Iversen, T., Kirkevaag, A., Seland, O., et al. (2013). The Norwegian Earth System Model, NorESM1-M - Part 1: Description and basic evaluation. *Geoscientific Model Development Discussions*, *5*, 2843–2931. https://doi.org/10.5194/gmdd-5-2843-2012

Beszczynska-Möller, A., Fahrbach, E., Schauer, U., & Hansen, E. (2012). Variability in Atlantic water temperature and transport at the entrance to the Arctic Ocean, 1997-2010. *ICES Journal of Marine Science*, *69*, 852–863. https://doi.org/10.1093/icesjms/fss056

Acknowledgments
The first author is particularly grateful to Prof. John Marshall and Prof. Helge Drange for constructive discussions and comments that helped to improve the manuscript, Evangelia Efstathiou for good suggestions, and the consortium supporting the development of the NorESM model. M. M. and L. H. S. were supported by the Centre for Climate Dynamics at the Bjerknes Centre for Climate Research, funded by the Norwegian Research Council. M. I. was partially supported by the ITU (ITU-TGA-2017-40657). Computing resources used in this work for ITU was provided by the National Center for High Performance Computing of Turkey (UHeM) under Grant 5004782017. R. Gelderloos and TWNH were financially supported by NOAA Grant NA15OAR4310172. C. L., C. T., and V. H. were supported through the projects ArcticMix, supported by the Copernicus Marine Environment Monitoring Service (CMEMS), and FREDY, supported by the French LEFE/INSU program. Q. W. was supported by the Helmholtz Climate Initiative REKLIM. T. K. and R. Gerdes are supported by the cooperative project 03F0729E (RACE II, Regional Atlantic Circulation and Global Climate), funded by the German Federal Ministry for Education and Research (BMBF). R. G. gratefully acknowledges funding by the Deutsche Forschungsgemeinschaft (DFG, German Research Foundation), Projektnummer 268020496, TRR 172, within the Transregional Collaborative Research Center "ArctiC Amplification: Climate Relevant Atmospheric and SurfaCe Processes, and Feedback Mechanisms" (AC). S. C., H. J., and Y. K. are grateful for funding from the U.K. Natural Environment Research Council, via the UK-OSNAP project (NE/K010948/1) and a DTP studentship. The HiGEM coupled climate model data are available from NERC's Centre for Environmental Data Analysis (CEDA; http://badc.nerc.ac.uk). This model was developed from the Met Office Hadley Centre Model by the U.K. High-Resolution Modelling (HiGEM) Project and the U.K. Japan Climate Collaboration (UJCC). HiGEM was supported by a NERC High Resolution Climate Modelling Grant (R8/H12/123). UJCC was supported by the Foreign and Commonwealth Office Global Opportunities Fund, and jointly funded by NERC and the DECC/Defra Met Office Hadley Centre Climate Programme (GA01101). The HiGEM model integrations were performed using the Japanese Earth Simulator supercomputer, supported by JAMSTEC. The work of Pier Luigi Vidale and Malcolm Roberts in leading the effort in Japan is particularly

valued. The Alberta team gratefully acknowledge the financial and logistic support of grants from the Natural Sciences and Engineering Research Council (NSERC) of Canada (RGPIN 04357 and RGPCC 433898), as well as Polar Knowledge Canada (PKC-NST-1617-0003). We are grateful to the NEMO development team and the Drakkar project for providing the model and continuous guidance and to Westgrid and Compute Canada for computational resources. For more details on the Alberta configuration, visit http://knossos.eas.ualberta.ca/anha/anhatable.php. An extracted set of time series from the various model simulations that have been used to make the figures are made available on the Bjerknes Climate Data Center (https://www.bcdc.no/).

Blanke, B., & Delecluse, P. (1993). Variability of the tropical Atlantic Ocean simulated by a general circulation model with two different mixed-layer physics. *Journal of Physical Oceanography*, *23*(7), 1363–1388. https://doi.org/10.1175/1520-0485(1993)023h1363:VOTTAOi2.0.CO;2

Brauch, J. P., & Gerdes, R. (2005). Response of the northern North Atlantic and Arctic oceans to a sudden change of the North Atlantic Oscillation. *Journal of Geophysical Research*, *110*, C11018. https://doi.org/10.1029/2004JC002436

Brodeau, L., Barnier, B., Treguier, A.-M., Penduff, T., & Gulev, S. (2010). An ERA40-based atmospheric forcing for global ocean circulation models. *Ocean Modelling*, *31*(3-4), 88–104. https://doi.org/10.1016/j.ocemod.2009.10.005

Carmack, E., Polyakov, I., Padman, L., Fer, I., Hunke, E., Hutchings, J., et al. (2015). Towards quantifying the increasing role of oceanic heat in sea ice loss in the New Arctic. *Bulletin of the American Meteorological Society*, *96*(12), 2079–2105. https://doi.org/10.1175/BAMS-D-13-00177.1

Cavalieri, D. J., & Parkinson, C. L. (2012). Arctic sea ice variability and trends, 1979–2010. *Cryosphere*, *6*(4), 881–889. https://doi.org/10.5194/tc-6-881-2012

Cavalieri, D., Parkinson, C., Gloersen, P., & Zwally, H. J. (1996). *Sea ice concentrations from Nimbus-7 SMMR and DMSP SSM/I-SSMIS passive microwave data, Version 1*. Boulder, CO: NASA National Snow and Ice Data Center Distributed Active Archive Center. https://doi.org/10.5067/8GQ8LZQVL0VL

Chatterjee, S., Raj, R. P., Bertino, L., Skagseth, R. M., & Johannessen, O. M. (2018). Role of Greenland Sea gyre circulation on Atlantic water temperature variability in the Fram Strait. *Geophysical Research Letters*, *45*, 8399–8406. https://doi.org/10.1029/2018GL079174

Cohen, J., Screen, J. A., Furtado, J. C., Barlow, M., Whittleston, D., Coumou, D., et al. (2014). Recent Arctic amplification and extreme mid-latitude weather. *Nature Geoscience*, *7*(9), 627. https://doi.org/10.1038/NGEO2234

Curry, R. G., & McCartney, M. S. (2001). Ocean gyre circulation changes associated with the North Atlantic Oscillation. *Journal of Physical Oceanography*, *31*(12), 3374–3400. https://doi.org/10.1175/1520-0485(2001)031h3374:OGCCAWi2.0.CO;2

Curry, J. A., Schramm, J. L., & Ebert, E. E. (1995). Sea ice-albedo climate feedback mechanism. *Journal of Climate*, *8*(2), 240–247. https://doi.org/10.1175/1520-0442(1995)008h0240:SIACFMi2.0.CO;2

Czaja, A., & Marshall, J. (2001). Observation of atmosphere ocean coupling in the North Atlantic. *Quarterly Journal of Royal Meteorological Soceity*, *127*(December 2000), 1893–1916. https://doi.org/10.1002/qj.49712757603

Dai, A., Qian, T., Trenberth, K. E., & Milliman, J. D. (2009). Changes in continental freshwater discharge from 1948 to 2004. *Journal of Climate*, *22*(10), 2773–2792. https://doi.org/10.1175/2008JCLI2592.1

Dai, A., & Trenberth, K. E. (2002). Estimates of freshwater discharge from continents: Latitudinal and seasonal variations. *Journal of Hydrometeorology*, *3*(6), 660–687. https://doi.org/10.1175/1525-7541(2002)003h0660:EOFDFCi2.0.CO;2

Dalpadado, P., Arrigo, K. R., Hjøllo, S. S., Rey, F., Ingvaldsen, R. B., Sperfeld, E., et al. (2014). Productivity in the Barents Sea—Response to recent climate variability. *PLoS ONE*, *9*(5), e95273. https://doi.org/10.1371/journal.pone.0095273

Danabasoglu, G., Yeager, S. G., Bailey, D., Behrens, E., Bentsen, M., Bi, D., et al. (2014). North Atlantic simulations in coordinated ocean-ice reference experiments phase II (CORE-II). Part I: Mean states. *Ocean Modelling*, *73*, 76–107. https://doi.org/10.1016/j.ocemod.2013.10.005

Danilov, S., Kivman, G., & Schröter, J. (2004). A finite-element ocean model: Principles and evaluation. *Ocean Modelling*, *6*(2), 125–150. https://doi.org/10.1016/S1463-5003(02)00063-X

Danilov, S., Wang, Q., Timmermann, R., Iakovlev, N., Sidorenko, D., Kimmritz, M., et al. (2015). Finite-element sea ice model (FESIM), version 2. *Geoscientific Model Development*, *8*(6), 1747–1761. https://doi.org/10.5194/gmd-8-1747-2015

Dee, D. P., Uppala, S. M., Simmons, A. J., Berrisford, P., Poli, P., Kobayashi, S., et al. (2011). The ERA-Interim reanalysis: Configuration and performance of the data assimilation system. *Quarterly Journal of the Royal Meteorological Society*, *137*(656), 553–597. https://doi.org/10.1002/qj.828

Dickson, R. R., Osborn, T. J., Hurrell, J. W., Meincke, J., Blindheim, J., Adlandsvik, B., et al. (2000). The Arctic Ocean response to the North Atlantic oscillation. *Journal of Climate*, *13*(15), 2671–2696. https://doi.org/10.1175/1520-0442(2000)013h2671:TAORTTi2.0.CO;2

Dunne, J. P., John, J. G., Adcroft, A. J., Griffies, S. M., Hallberg, R. W., Shevliakova, E., et al. (2012). GFDL's ESM2 global coupled climate-carbon earth system models. Part I: Physical formulation and baseline simulation characteristics. *Journal of Climate*, *25*(19), 6646–6665. https://doi.org/10.1175/JCLI-D-11-00560.1

Eden, C., & Jung, T. (2001). North Atlantic interdecadal variability: Oceanic response to the North Atlantic oscillation (1865-1997). *Journal of Climate*, *14*(5), 676–691. https://doi.org/10.1175/1520-0442(2001)014h0676:NAIVORi2.0.CO;2

Farneti, R., Downes, S. M., Griffies, S. M., Marsland, S. J., Behrens, E., Bentsen, M., et al. (2015). An assessment of Antarctic Circumpolar Current and Southern Ocean meridional overturning circulation during 1958-2007 in a suite of interannual CORE-II simulations. *Ocean Modelling*, *93*, 84–120. https://doi.org/10.1016/j.ocemod.2015.07.009

Fox-Kemper, B., Ferrari, R., & Hallberg, R. (2008). Parameterization of mixed layer eddies. Part I: Theory and diagnosis. *Journal of Physical Oceanography*, *38*(6), 1145–1165. https://doi.org/10.1175/2007JPO3792.1

Furevik, T. (2001). Annual and interannual variability of Atlantic Water temperatures in the Norwegian and Barents Seas: 1980-1996. *Deep-Sea Research Part I: Oceanographic Research Papers*, *48*(2), 383–404. https://doi.org/10.1016/S0967-0637(00)00050-9

Gent, P. R., & Mcwilliams, J. C. (1990). Isopycnal mixing in ocean circulation models. *Journal of Physical Oceanography*, *20*(1), 150–155. https://doi.org/10.1175/1520-0485(1990)020h0150:IMIOCMi2.0.CO;2

Gregory, J. M., Andrews, T., & Good, P. (2015). The inconstancy of the transient climate response parameter under increasing CO2. *Philosophical Transactions of the Royal Society A: Mathematical, Physical and Engineering Sciences*, *373*(2054), 20140417. https://doi.org/10.1098/rsta.2014.0417

Griffies, S. M. (2012). Elements of the modular ocean model (MOM). GFDL Ocean Group Tech. Rep, 7, 620.

Griffies, S. M., Winton, M., Samuels, B., Danabasoglu, G., Yeager, S., Marsland, S., et al. (2012). Datasets and protocol for the CLIVAR WGOMD Coordinated Ocean-sea ice Reference Experiments (COREs). WCRP Report, 21, 1–21.

Griffies, S. M., Yin, J., Durack, P. J., Goddard, P., Bates, S. C., Behrens, E., et al. (2014). An assessment of global and regional sea level for years 1993–2007 in a suite of interannual CORE-II simulations. *Ocean Modelling*, *78*, 35–89.

Grotefendt, K., Logemann, K., Quadfasel, D., & Ronski, S. (1998). Is the Arctic Ocean warming? *Journal of Geophysical Research*, *103*(C12), 27679. https://doi.org/10.1029/98JC02097

Haine, ThomasW. N., Curry, B., Gerdes, R., Hansen, E., Karcher, M., Lee, C., et al. (2015). Arctic freshwater export: Status, mechanisms, and prospects. *Global and Planetary Change*, *125*, 13–35. https://doi.org/10.1016/j.gloplacha.2014.11.013

Hattermann, T., Isachsen, P. E., Von Appen, W. J., Albretsen, J., & Sundfjord, A. (2016). Eddy-driven recirculation of Atlantic Water in Fram Strait. *Geophysical Research Letters*, *43*, 3406–3414. https://doi.org/10.1002/2016GL068323

He, Y. C., Drange, H., Gao, Y., & Bentsen, M. (2016). Simulated Atlantic Meridional Overturning Circulation in the 20th century with an ocean model forced by reanalysis-based atmospheric data sets. *Ocean Modelling*, *100*, 31–48. https://doi.org/10.1016/j.ocemod.2015.12.011

Helland-Hansen, B., & Nansen, F. (1909). *The Norwegian Sea: Its physical oceanography based upon the Norwegian researches 1900-1904*. Kristiania: Det Mallingske bogtrykkeri.

Hinzman, L. D., Deal, C. J., Mcguire, A. D., Mernild, S. H., Polyakov, I. V., & Walsh, J. E. (2013). Trajectory of the Arctic as an integrated system. *Ecological Applications*, *23*(8), 1837–1868. https://doi.org/10.1890/11-1498.1

Holliday, N. P., Hughes, S. L., Bacon, S., Beszczynska-Möller, A., Hansen, B., Lavín, A., et al. (2008). Reversal of the 1960s to 1990s freshening trend in the northeast North Atlantic and Nordic Seas. *Geophysical Research Letters*, *35*, L03614. https://doi.org/10.1029/2007GL032675

Holloway, G. (1987). Systematic forcing of large-scale geophysical flows by eddy-topography interaction. *Journal of Fluid Mechanics*, *184*, 463–476. https://doi.org/10.1017/S0022112087002970

Holloway, G., Dupont, F., Golubeva, E., Häkkinen, S., Hunke, E., Jin, M., et al. (2007). Water properties and circulation in Arctic Ocean models. *Journal of Geophysical Research*, *112*, 1–18. https://doi.org/10.1029/2006JC003642

Hurrell, J. W. (1995). Decadal trends in the North Atlantic Oscillation: Regional temperatures and precipitation. *Science*, *269*(5224), 676–679. https://doi.org/10.1126/science.269.5224.676

IPCC (2014). *Climate Change 2013—The Physical Science Basis: Working Group I Contribution to the Fifth Assessment Report of the Intergovernmental Panel on Climate Change*. Cambridge: Cambridge University Press. https://doi.org/10.1017/CBO9781107415324

Ikeda, M. (1990). Decadal oscillations of the air-ice-ocean system in the Northern Hemisphere. *Atmosphere-Ocean*, *28*(1), 106–139. https://doi.org/10.1080/07055900.1990.9649369

Ikeda, M., Wang, J., & Zhao, J. (2001). Hypersensitive decadal oscillations in the Arctic/subarctic climate. *Geophysical research letters*, *28*(7), 1275–1278. https://doi.org/10.1029/2000GL011773

Ilicak, M., Drange, H., Wang, Q., Gerdes, R., Aksenov, Y., Bailey, D., et al. (2016). An assessment of the Arctic Ocean in a suite of interannual CORE-II simulations. Part III: Hydrography and fluxes. *Ocean Modelling*, *100*, 141–161. https://doi.org/10.1016/j.ocemod.2016.02.004

Ingvaldsen, R. (2004). The Atlantic inflow to the Barents Sea. *Continental Shelf Research*, *10*(1), 5817. https://doi.org/10.1029/2001JC001039.Ottersen

Ingvaldsen, R. B., Asplin, L., & Loeng, H. (2004). Velocity field of the western entrance to the Barents Sea. *Journal of Geophysical Research*, *109*, 1–12. https://doi.org/10.1029/2003JC001811

Isachsen, P. E., LaCasce, J. H., Mauritzen, C., & Hakkinen, S. (2003). Wind-driven variability of the large-scale recirculating flow in the Nordic Seas and Arctic Ocean. *Journal of Physical Oceanography*, *33*(12), 2534–2550. https://doi.org/10.1175/1520-0485(2003)033h2534:WVOTLRi2.0.CO;2

Ivanov, V., Alexeev, V., Koldunov, N. V., Repina, I., Sando, A. B., Smedsrud, L. H., & Smirnov, A. (2016). Arctic Ocean heat impact on regional ice decay - a suggested positive feedback. *Journal of Physical Oceanography*, *46*(5), 1437–1456. https://doi.org/10.1175/JPO-D-15-0144.1

Ivanov, B. V., Gerland, S., Winther, J.-G., & Goodwin, H. (2003). Energy exchange processes in the marginal ice zone of the Barents Sea, Arctic Ocean, during spring 1999. *Journal of Glaciology*, *49*(166), 415–419. https://doi.org/10.3189/172756503781830557

Jahnke-Bornemann, A., & Brümmer, B. (2009). The Iceland-Lofotes pressure difference: Different states of the North Atlantic low-pressure zone. *Tellus, Series A: Dynamic meteorology and oceanography*, *61*(4), 466–475. https://doi.org/10.1111/j.1600-0870.2009.00401.x

Jakobsson, M., & Macnab, R. (2006). A comparison between GEBCO Sheet 5.17 and the International Bathymetric Chart of the Arctic Ocean (IBCAO) version 1.0. *Marine Geophysical Researches*, *27*(1), 35–48. https://doi.org/10.1007/s11001-005-7760-0

Johnson, H. L., Cornish, S. B., Kostov, Y., Beer, E., & Lique, C. (2018). Arctic Ocean freshwater content and its decadal memory of sea-level pressure. *Geophysical Research Letters*, *45*, 4991–5001. https://doi.org/10.1029/2017GL076870

Jungclaus, J. H., Fischer, N., Haak, H., Lohmann, K., Marotzke, J., Matei, D., et al. (2013). Characteristics of the ocean simulations in the Max Planck Institute Ocean Model (MPIOM) the ocean component of the MPI Earth system model. *Journal of Advances in Modeling Earth Systems*, *5*, 422–446. https://doi.org/10.1002/jame.20023

Karcher, M., Kauker, F., Gerdes, R., Hunke, E., & Zhang, J. (2007). On the dynamics of Atlantic Water circulation in the Arctic Ocean. *Journal of Geophysical Research*, *112*, C04S02. https://doi.org/10.1029/2006JC003630

Karcher, M., Smith, J. N., Kauker, F., Gerdes, R., & Smethie, W. M. (2012). Recent changes in Arctic Ocean circulation revealed by iodine-129 observations and modeling. *Journal of Geophysical Research*, *117*, C08007. https://doi.org/10.1029/2011JC007513

Kostov, Y., Marshall, J., Hausmann, U., Armour, K. C., Ferreira, D., & Holland, M. M. (2017). Fast and slow responses of Southern Ocean sea surface temperature to SAM in coupled climate models. *Climate Dynamics*, *48*(5-6), 1595–1609. https://doi.org/10.1007/s00382-016-3162-z

Kwok, R. (2018). Arctic sea ice thickness, volume, and multiyear ice coverage: Losses and coupled variability (1958-2018). *Environmental Research Letters*, *13*(10), 105005. https://doi.org/10.1088/1748-9326/aae3ec

Langehaug, H. R., Medhaug, I., Eldevik, T., & Otterå, O. H. (2012). Arctic/Atlantic exchanges via the subpolar gyre. *Journal of Climate*, *25*(7), 2421–2439. https://doi.org/10.1175/JCLI-D-11-00085.1

Large, W. G., McWilliams, J. C., & Doney, S. C. (1994). Oceanic vertical mixing: A review and a model with a nonlocal boundary layer parameterization. *Reviews of Geophysics*, *32*(4), 363–403. https://doi.org/10.1029/94RG01872

Levitus, S., Matishov, G., Seidov, D., & Smolyar, I. (2009). Barents Sea multidecadal variability. *Geophysical Research Letters*, *36*, L19604. https://doi.org/10.1029/2009GL039847

Li, D., Zhang, R., & Knutson, T. R. (2017). On the discrepancy between observed and CMIP5 multi-model simulated Barents Sea winter sea ice decline. *Nature Communications*, *8*, 1–7. https://doi.org/10.1038/ncomms14991

Lien, V. S., Schlichtholz, P., Skagseth, Ø., & Vikebø, F. B. (2017). Wind-Driven Atlantic Water Flow as a Direct Mode for Reduced Barents Sea Ice Cover. *Journal of Climate*, *30*(2), 803–812. https://doi.org/10.1175/JCLI-D-16-0025.1

Lien, V. S., Vikebø, F. B., & Skagseth, Ø. (2013). One mechanism contributing to co-variability of the Atlantic inflow branches to the Arctic. *Nature Communications*, *4*, 1–6. https://doi.org/10.1038/ncomms2505

Lind, S., & Ingvaldsen, R. B. (2012). Variability and impacts of Atlantic Water entering the Barents Sea from the north. *Deep-Sea Research Part I: Oceanographic Research Papers*, *62*, 70–88. https://doi.org/10.1016/j.dsr.2011.12.007

Lind, S., Ingvaldsen, R. B., & Furevik, T. (2016). Arctic layer salinity controls heat loss from deep Atlantic layer in seasonally ice-covered areas of the Barents Sea. *Geophysical Research Letters*, *43*, 5233–5242. https://doi.org/10.1002/2016GL068421

Lind, S., Ingvaldsen, R. B., & Furevik, T. (2018). Sea linked to declining sea-ice import. *Nature Climate Change*, *8*(634), 634–639. https://doi.org/10.1038/s41558-018-0205-y

Liptak, J., & Strong, C. (2014). The winter atmospheric response to sea ice anomalies in the Barents Sea. *Journal of Climate*, *27*(2), 914–924. https://doi.org/10.1175/JCLI-D-13-00186.1

Lique, C., Johnson, H. L., & Davis, P. E. D. (2015). On the interplay between the circulation in the surface and the intermediate layers of the Arctic Ocean. *Journal of Physical Oceanography*, *45*(5), 1393–1409. https://doi.org/10.1175/JPO-D-14-0183.1

Lohmann, K., Drange, H., & Bentsen, M. (2009). Response of the North Atlantic subpolar gyre to persistent North Atlantic oscillation like forcing. *Climate Dynamics*, *32*(2-3), 273–285. https://doi.org/10.1007/s00382-008-0467-6

Madec, G. (2014). NEMO ocean engine (*27*). Institut Pierre-Simon Laplace.

Marnela, M., Rudels, B., Houssais, M. N., Beszczynska-Möller, A., & Eriksson, P. B. (2013). Recirculation in the Fram Strait and transports of water in and north of the Fram Strait derived from CTD data. *Ocean Science*, *9*(3), 499–519. https://doi.org/10.5194/os-9-499-2013

Marshall, J., Adcroft, A., Hill, C., Perelman, L., & Heisey, C. (1997). A finite-volume, incompressible Navier Stokes model for studies of the ocean on parallel computers. *Journal of Geophysical Research*, *102*(C3), 5753–5766. https://doi.org/10.1029/96JC02775

Marshall, J., Armour, K. C., Scott, J. R., Kostov, Y., Hausmann, U., Ferreira, D., et al. (2014). The ocean's role in polar climate change: asymmetric Arctic and Antarctic responses to greenhouse gas and ozone forcing. *Philosophical Transactions of the Royal Society A*, *372*, 20130040. https://doi.org/10.1098/rsta.2013.0040

Marshall, J., Scott, J., & Proshutinsky, A. (2017). Climate Response Functions for the Arctic Ocean: a proposed coordinated modeling experiment. *Geoscientific Model Development Discussions*, *10*(January), 1–25. https://doi.org/10.5194/gmd-2016-316

Masina, S., Storto, A., Ferry, N., Valdivieso, M., Haines, K., Balmaseda, M., et al. (2015). An ensemble of eddy-permitting global ocean reanalyses from the MyOcean project. *Climate Dynamics*, *49*(3), 813–841. https://doi.org/10.1007/s00382-015-2728-5

Medhaug, I., Langehaug, H. R., Eldevik, T., Furevik, T., & Bentsen, M. (2012). Mechanisms for decadal scale variability in a simulated Atlantic meridional overturning circulation. *Climate Dynamics*, *39*(1-2), 77–93. https://doi.org/10.1007/s00382-011-1124-z

Meneghello, G., Marshall, J., Campin, J.-M., Doddridge, E., & Timmermans, M.-L. (2018). The Ice-Ocean governor: ice-ocean stress feedback limits Beaufort Gyre spin up. *Geophysical Research Letters*, *45*, 293–299. https://doi.org/10.1029/2018GL080171

Montgomery, R. B. (1974). Comments on seasonal variability of Florida Current-Niiler and Richardson. *Journal of Marine Research*, *32*(3), 533–534.

Moore, G. W. K., Renfrew, I. A., & Pickart, R. S. (2012). Spatial distribution of air-sea heat fluxes over the sub-polar North Atlantic Ocean. *Geophysical Research Letters*, *39*, L18806. https://doi.org/10.1029/2012GL053097

Moore, G. W. K., Renfrew, I. A., & Pickart, R. S. (2013). Multidecadal mobility of the north atlantic oscillation. *Journal of Climate*, *26*(8), 2453–2466. https://doi.org/10.1175/JCLI-D-12-00023.1

Moss, R. H., Edmonds, J. A., Hibbard, K. A., Manning, M. R., Rose, S. K., Van Vuuren, D. P., et al. (2010). The next generation of scenarios for climate change research and assessment. *Nature*, *463*(7282), 747. https://doi.org/10.1038/nature08823

Muilwijk, M., Smedsrud, L. H., Ilicak, M., & Drange, H. (2018). Atlantic Water heat transport variability in the 20th century Arctic Ocean from a global ocean model and observations. *Journal of Geophysical Research: Oceans*, *123*, 8159–8179. https://doi.org/10.1029/2018JC014327

Nakanowatari, T., Sato, K., & Inoue, J. (2014). Predictability of the Barents Sea ice in early winter: Remote effects of oceanic and atmospheric thermal conditions from the North Atlantic. *Journal of Climate*, *27*(23), 8884–8901. https://doi.org/10.1175/JCLI-D-14-00125.1

Nøst, O. A., & Isachsen, P. E. (2003). The large-scale time-mean ocean circulation in the Nordic Seas and Arctic Ocean estimated from simplified dynamics. *Journal of Marine Research*, *61*(2), 175–210. https://doi.org/10.1357/002224003322005069

Onarheim, I. H., & Arthun, M. (2017). Toward an ice-free Barents Sea. *Geophysical Research Letters*, *44*, 8387–8395. https://doi.org/10.1002/2017GL074304

Onarheim, I. H., Eldevik, T., Årthun, M., Ingvaldsen, R. B., & Smedsrud, L. H. (2015). Skillful prediction of Barents Sea ice cover. *Geophysical Research Letters*, *42*, 5364–5371. https://doi.org/10.1002/2015GL064359

Onarheim, I. H., Eldevik, T., Smedsrud, L. H., & Stroeve, J. C. (2018). Seasonal and regional manifestation of Arctic sea ice loss. *Journal of Climate*, *31*(12), 4917–4932. https://doi.org/10.1175/JCLI-D-17-0427.1

Onarheim, I. H., Smedsrud, L. H., Ingvaldsen, R. B., & Nilsen, F. (2014). Loss of sea ice during winter north of Svalbard. *Tellus A*, *66*(1), 23933. https://doi.org/10.3402/tellusa.v66.23933

Onogi, K., Tsutsui, J., Koide, H., Sakamoto, M., Kobayashi, S., Hatsushika, H., et al. (2007). The JRA-25 reanalysis. *Journal of the Meteorological Society of Japan. Ser. II*, *85*(3), 369–432. https://doi.org/10.2151/jmsj.85.369

Orvik, K. A., & Skagseth, O. (2003). The impact of the wind stress curl in the North Atlantic on the Atlantic inflow to the Norwegian Sea toward the Arctic. *Geophysical Research Letters*, *30*(17), 1884. https://doi.org/10.1029/2003GL017932

Orvik, K. A., Skagseth, O., & Mork, M. (2001). Atlantic inflow to the Nordic Seas: Current structure and volume fluxes from moored current meters, VM-ADCP and SeaSoar-CTD observations, 1995-1999. *Deep-Sea Research Part I: Oceanographic Research Papers*, *48*(4), 937–957. https://doi.org/10.1016/S0967-0637(00)00038-8

Pérez-Hernández, M., S. Pickart, R., Torres, D., Bahr, F., Sundfjord, A., Ingvaldsen, R., et al. (2019). Structure, Transport, and Seasonality of the Atlantic Water Boundary Current North of Svalbard: Results From a Yearlong Mooring Array. *Journal of Geophysical Research: Oceans*, *124*, 1679–1698. https://doi.org/10.1029/2018JC014759

Pacanowski, R. C., & Philander, S. G. H. (1981). Parameterization of vertical mixing in numerical models of tropical oceans. *Journal of Physical Oceanography*, *11*(11), 1443–1451. https://doi.org/10.1175/1520-0485(1981)011h1443:POVMINi2.0.CO;2

Peralta-Ferriz, C., Morison, J. H., Wallace, J. M., Bonin, J. A., & Zhang, J. (2014). Arctic ocean circulation patterns revealed by GRACE. *Journal of Climate*, *27*(4), 1445–1468. https://doi.org/10.1175/JCLI-D-13-00013.1

Perovich, D. K., & Richter-Menge, J. A. (2015). Regional variability in sea ice melt in a changing Arctic. *Philosophical Transactions of the Royal Society A: Mathematical, Physical and Engineering Sciences*, *373*(2045), 20140165. https://doi.org/10.1098/rsta.2014.0165

Peterson, A. K., Fer, I., McPhee, M. G., & Randelhoff, A. (2017). Turbulent heat and momentum fluxes in the upper ocean under Arctic sea ice. *Journal of Geophysical Research: Oceans*, *122*, 1439–1456. https://doi.org/10.1002/2016JC012283

Polyakov, I. V., Pnyushkov, A. V., Alkire, M. B., Ashik, I. M., Baumann, T. M., Carmack, E. C., et al. (2017). Greater role for Atlantic inflows on sea-ice loss in the Eurasian Basin of the Arctic Ocean. *Science*, *291*(April), 285–291. https://doi.org/10.1126/science.aai8204

Rudels, B., Anderson, L. G., & Jones, E. P. (1996). Formation and evolution of the surface mixed layer and halocline of the Arctic Ocean. *Journal of Geophysical Research*, *101*, 8807–8821. https://doi.org/10.1029/96JC00143

Saha, S., Moorthi, S., Pan, H.-L., Wu, X., Wang, J., Nadiga, S., et al. (2010). The NCEP climate forecast system reanalysis. *Bulletin of the American Meteorological Society*, *91*(8), 1015–1058. https://doi.org/10.1175/2010BAMS3001.1

Sandø, A, Gao, Y., & Langehaug, H. R. (2014). Poleward ocean heat transport, sea ice processes, and Arctic sea ice variability in NorESM1-M simulations. *Journal of Geophysical Research: Oceans*, *119*, 2095–2108. https://doi.org/10.1002/2013JC009435

Sandø, A. B., Nilsen, J. E., Gao, Y., & Lohmann, K. (2010). Importance of heat transport and local air-sea heat fluxes for Barents Sea climate variability. *Journal of Geophysical Research*, *115*, C07013. https://doi.org/10.1029/2009JC005884

Schauer, U. (2004). Arctic warming through the Fram Strait: Oceanic heat transport from 3 years of measurements. *Journal of Geophysical Research*, *109*, C06026. https://doi.org/10.1029/2003JC001823

Schauer, U., & Beszczynska-Möller, A. (2009). Problems with estimation and interpretation of oceanic heat transport-conceptual remarks for the case of Fram Strait in the Arctic Ocean. *Ocean Science*, *5*(4), 487–494. https://doi.org/10.5194/os-5-487-2009

Schauer, U., Loeng, H., Rudels, B., Ozhigin, V. K., & Dieck, W. (2002). Atlantic Water flow through the Barents and Kara Seas. *Deep Sea Research Part I: Oceanographic Research Papers*, *49*(12), 2281–2298. https://doi.org/10.1016/S0967-0637(02)00125-5

Schlichtholz, P., & Houssais, M. N. (2011). Forcing of oceanic heat anomalies by air-sea interactions in the Nordic Seas area. *Journal of Geophysical Research*, *116*, 1–21. https://doi.org/10.1029/2009JC005944

Screen, J. A., & Simmonds, I. (2010). The central role of diminishing sea ice in recent Arctic temperature amplification. *Nature*, *464*(7293), 1334–1337. https://doi.org/10.1038/nature09051

Serreze, M. C., & Barry, R. G. (2011). Processes and impacts of Arctic amplification: A research synthesis. *Global and Planetary Change*, *77*(1-2), 85–96. https://doi.org/10.1016/j.gloplacha.2011.03.004

Serreze, M. C., Holland, M. M., & Stroeve, J. (2007). Perspectives on the Arctic's shrinking sea-ice cover. *Science*, *315*(5818), 1533–1536. https://doi.org/10.1126/science.1139426

Shaffrey, LCoauthors, Stevens, I., Norton, WA, Roberts, MJ, Vidale, P. L., Harle, JD, et al. (2009). UK HiGEM: The new UK high-resolution global environment model—Model description and basic evaluation. *Journal of Climate*, *22*(8), 1861–1896. https://doi.org/10.1175/2008JCLI2508.1

Skagseth, Ø., Drinkwater, K. F., & Terrile, E. (2011). Wind-and buoyancy-induced transport of the Norwegian Coastal Current in the Barents Sea. *Journal of Geophysical Research*, *116*, C08007. https://doi.org/10.1029/2011JC006996

Skagseth, Ø., Furevik, T., Ingvaldsen, R. B., Loeng, H., Mork, K. A., Orvik, K. A., & Ozhigin, V. (2008). Volume and heat transports to the Arctic Ocean via the Norwegian and Barents Seas. In *Arctic-Subarctic Ocean Fluxes: Defining the role of the Northern Seas in Climate* (pp. 45–64). Dordrecht: Springer.

Smedsrud, L. H., Esau, I., Ingvaldsen, R. B., Eldevik, T., Haugan, P. M., Li, C., et al. (2013). The role of the Barents Sea in the Arctic climate system. *Reviews of Geophysics*, *51*, 415–449. https://doi.org/10.1002/rog.20017

Smedsrud, L. H., Ingvaldsen, R., Nilsen, J. E. Ø., & Skagseth, Ø (2010). Heat in the Barents Sea: Transport, storage, and surface fluxes. *Ocean Science*, *6*(1), 219–234. https://doi.org/10.5194/os-6-219-2010

Smith, G. C., Roy, F., Mann, P., Dupont, F., Brasnett, B., Lemieux, J., et al. (2014). A new atmospheric dataset for forcing ice-ocean models: Evaluation of reforecasts using the Canadian global deterministic prediction system. *Quarterly Journal of the Royal Meteorological Society*, *140*(680), 881–894. https://doi.org/10.1002/qj.2194

Sorokina, S. A., Li, C., Wettstein, J. J., & Kvamstø, N. G. (2016). Observed atmospheric coupling between Barents Sea ice and the warm-Arctic cold-Siberian anomaly pattern. *Journal of Climate*, *29*(2), 495–511. https://doi.org/10.1175/JCLI-D-15-0046.1

Steiner, N., Holloway, G., Gerdes, R., Häkkinen, S., Holland, D., Karcher, M., et al. (2004). Comparing modeled streamfunction, heat and freshwater content in the Arctic Ocean. *Ocean Modelling*, *6*(3-4), 265–284. https://doi.org/10.1016/S1463-5003(03)00013-1

Stewart, K. D., & Haine, T. W. N. (2013). Wind-driven Arctic freshwater anomalies. *Geophysical Research Letters*, *40*, 6196–6201. https://doi.org/10.1002/2013GL058247

Tesdal, J.-E., Abernathey, R. P., Goes, J. I., Gordon, A. L., & Haine, T. W. N. (2018). Salinity trends within the upper layers of the subpolar North Atlantic. *Journal of Climate*, *31*(7), 2675–2698. https://doi.org/10.1175/JCLI-D-17-0532.1

Thoma, M., Gerdes, R., Greatbatch, R. J., & Ding, H. (2015). Partially coupled spin-up of the MPI-ESM: Implementation and first results. *Geoscientific Model Development*, *8*(1), 51–68. https://doi.org/10.5194/gmd-8-51-2015

Thompson, D. W., & Wallace, J. M. (1998). The Arctic oscillation signature in the wintertime geopotential height and temperature fields. *Geophysical Research Letters*, *25*(9), 1297–1300. https://doi.org/10.1029/98GL00950

Venegas, S. A., & Mysak, L. A. (2000). Is there a dominant timescale of natural climate variability in the Arctic? *Journal of Climate*, *13*(19), 3412–3434. https://doi.org/10.1175/1520-0442(2000)013h3412:ITADTOi2.0.CO;2

Vihma, T. (2014). Effects of Arctic Sea ice decline on weather and climate: A review. *Surveys in Geophysics*, *35*(5), 1175–1214. https://doi.org/10.1007/s10712-014-9284

Visbeck, M., Chassignet, E., Curry, R. G., Delworth Thomas, D. R. R., & Krahmann, G. (2013). The ocean's response to North Atlantic Oscillation variability. In *The North Atlantic Oscillation: Climatic Significance and Environmental Impact* (pp. 113–145). Washington, DC: American Geophysical Union. https://doi.org/10.1029/134GM06

Visbeck, M., Cullen, H., Krahmann, G., & Naik, N. (1998). Ocean model's response to North Atlantic Oscillation-like wind forcing. *Geophysical Research Letters*, *25*(24), 4521–4524. https://doi.org/Doi10.1029/1998gl900162

Wang, Q., Danilov, S., & Schröter, J. (2008). Finite element ocean circulation model based on triangular prismatic elements, with application in studying the effect of topography representation. *Journal of Geophysical Research*, *113*, C05015. https://doi.org/10.1029/2007JC004482

Wang, Q., Danilov, S., Sidorenko, D., Timmermann, R., Wekerle, C., Wang, X., et al. (2014). The Finite Element Sea Ice-Ocean Model (FESOM) v. 1.4: Formulation of an ocean general circulation model. *Geoscientific Model Development*, *7*(2), 663–693. https://doi.org/10.5194/gmd-7-663-2014

Wang, Q., Ilicak, M., Gerdes, R., Drange, H., Aksenov, Y., Bailey, D. A., et al. (2016a). An assessment of the Arctic Ocean in a suite of interannual CORE-II simulations. Part II: Liquid freshwater. *Ocean Modelling*, *99*, 86–109. https://doi.org/10.1016/j.ocemod.2015.12.009

Wang, Q., Ilicak, M., Gerdes, R., Drange, H., Aksenov, Y., Bailey, D. A., et al. (2016b). An assessment of the Arctic Ocean in a suite of interannual CORE-II simulations. Part II: Liquid freshwater. *Ocean Modelling*, *99*, 86–109. https://doi.org/10.1016/j.ocemod.2015.12.009

Wang, Q., Marshall, J., Scott, J., Meneghello, G., Danilov, S., & Jung, T. (2019). On the feedback of ice-ocean stress coupling from geostrophic currents in an anticyclonic wind regime over the Beaufort Gyre. *Journal of Physical Oceanography*, *49*(2019), 369–383. https://doi.org/10.1175/JPO-D-18-0185.1

Wekerle, C., Wang, Q., Danilov, S., Schourup-Kristensen, V., von Appen, W.-J., & Jung, T. (2017). Atlantic Water in the Nordic Seas: Locally eddy-permitting ocean simulation in a global setup. *Journal of Geophysical Research: Oceans*, *122*, 914–940. https://doi.org/10.1002/2016JC012121

Wekerle, C., Wang, Q., von Appen, W., Danilov, S., Schourup-Kristensen, V., & Jung, T. (2017). Eddy-resolving simulation of the Atlantic Water circulation in the Fram Strait with focus on the seasonal cycle. *Journal of Geophysical Research: Oceans*, *122*, 8385–8405. https://doi.org/10.1002/2017JC012974

Yang, S., & Christensen, J. H. (2012). Arctic sea ice reduction and European cold winters in CMIP5 climate change experiments. *Geophysical Research Letters*, *39*, L20707. https://doi.org/10.1029/2012GL053338

Zhang, R. (2015). Mechanisms for low-frequency variability of summer Arctic sea ice extent. *Proceedings of the National Academy of Sciences*, *112*(15), 4570–4575. https://doi.org/10.1073/pnas.1422296112

Zhang, J., Lindsay, R., Steele, M., & Schweiger, A. (2008). What drove the dramatic retreat of arctic sea ice during summer 2007? *Geophysical Research Letters*, *35*, L11505. https://doi.org/10.1029/2008GL034005

Zhang, J., Rothrock, D. A., & Steele, M. (1998). Warming of the Arctic Ocean by a strengthened Atlantic inflow: Model results. *Geophysical Research Letters*, *25*(10), 1745–1748. https://doi.org/10.1029/98GL01299

Zhang, J., & Steele, M. (2007). Effect of vertical mixing on the Atlantic Water layer circulation in the Arctic Ocean. *Journal of Geophysical Research*, *112*, C04S04. https://doi.org/10.1029/2006JC003732